

An aerial satellite image of a river system, likely in a monsoon-affected region. The river is dark blue, winding through a landscape of green and brown. A black rectangular text box is overlaid on the upper left portion of the image.

# Combining microwave and optical remote sensing to monitor rivers in monsoon affected regions

M.H. Dooren

Technische Universiteit Delft



# Combining microwave and optical remote sensing to monitor rivers in monsoon affected regions

by

**M.H. Dooren**

to obtain the degree of Master of Science  
at the Delft University of Technology,  
to be defended publicly on 17 October 2019

Student number: 4297482  
Project duration: January, 2019 – October, 2019  
Thesis committee: Dr. S.L.M. Lhermitte, TU Delft, supervisor  
Dr. ir. C.J. Sloff, TU Delft, Deltares  
Dr. R.C. Lindenbergh, TU Delft  
Ir. Mark Hegnauer, Deltares  
Dr. ir. G.V. Donchyts, Deltares

An electronic version of this thesis is available at <http://repository.tudelft.nl/>



# ABSTRACT

Understanding the river dynamics is very important to be able to make use of all river functions and to protect ourselves against floods. Hydrodynamic models are used to predict river behaviour and one of the input parameters is the river geometry. In-situ measuring of river geometry can be very expensive and time consuming. Remote sensing offers a more efficient method to monitor rivers, because it has the ability to continuously monitor the Earth surface at multiple scales. Rivers in monsoon dominated regions show a strong seasonal variation in discharge and have a high variability in morphodynamics. Therefore it is very important to have a high spatial-temporal resolution of river geometry data as input for hydrodynamic models to keep up with the changes in the river. Both optical and microwave images can be used in providing information about the river geometry. The microwave images need a lot of processing to deal with noise, but they are not limited by clouds, whereas optical sensors are troubled by clouds but produce less noise. The benefit of combining these methods is because the microwave images could fill the gap of cloud covered optical images during the monsoon. The main result from this thesis is that more investigation is needed on how to deal with the noise produced by the microwave images before the methods can be combined. Nevertheless it is shown that using the Canny Edge detector and Otsu thresholding improves the results. With this research we are a small step further in global river monitoring. This is important in particular for parts of the world where rivers are not continuously monitored because they are situated in hard to reach terrain and because the country will not invest in local gauge stations. Having more knowledge about river behaviour will help to get a better understanding of water losses along the river course, habitat change and flood risks.



# PREFACE

This master thesis is the final product of my master Geoscience and Remote Sensing at the Technical University Delft. In this research an analysis is performed on how optical and microwave remote sensing can be combined to improve the spatial-temporal frequency of river geometry estimations for hydrodynamic modelling. I have written this thesis during an internship at Deltares, an institution for applied research in the field of water and subsurface.

During my master I have always been intrigued by how much possibilities satellites provide in monitoring the Earth and for my master thesis I wanted to explore those possibilities. At Deltares I got the opportunity to use this interest in monitoring river dynamics. Because my background knowledge about river dynamics was very limited, I followed both River Dynamics 1 and 2 courses from the hydraulic engineering department at the TU Delft to enhance my knowledge.

With this thesis I hope to make a small contribution to our knowledge in the possibilities we have by using satellites to monitor the Earth and in this case the river dynamics. Rivers are very important in our daily lives. Not only do we need the rivers for fresh water, but also they are necessary for transportation and keeping the ecosystem in balance. In this era when climate change has made its appearance, it is even more important to understand all river dynamics to be able to keep access to fresh water and to protect ourselves against floods.

From all people who helped me during the process of writing this thesis I would like to start with thanking my supervisors at Deltares for their guidance through the process of this research. Gennadii Donchyts provided me with a lot of Google Earth Engine scripts and helped me to understand them and work with them. Mark Hegnauer helped me a lot on the water management part of the thesis and Kees Sloff was the expert on morphodynamics and had been involved in other projects concerning the Irrawaddy river in Myanmar. Furthermore I would like to thank the other employees at Deltares who invited me for their weekly lunch run, but more importantly who were always willing to answer my questions and to share ideas on the topic. From the TU delft I want to thank, Stef Lhermite who was the head of the committee and Roderik Lindenbergh who joined the committee during the final stages of this thesis.

*M.H. Dooren  
Delft, October 2019*



# CONTENTS

<b>1</b>	<b>Introduction</b>	<b>1</b>
1.1	Context . . . . .	1
1.2	Problem Definition . . . . .	1
1.3	Research objective and Questions. . . . .	3
1.4	Thesis outline . . . . .	3
<b>2</b>	<b>Background</b>	<b>5</b>
2.1	River definition . . . . .	5
2.2	1D Hydrodynamic modelling . . . . .	6
2.3	Remote Sensing. . . . .	7
2.4	Surface water detection . . . . .	11
2.5	Image processing . . . . .	13
<b>3</b>	<b>The Irrawaddy River</b>	<b>15</b>
3.1	Location and background. . . . .	15
3.2	Data availability. . . . .	16
<b>4</b>	<b>Methodology</b>	<b>19</b>
4.1	Image selection . . . . .	19
4.2	Resampling . . . . .	21
4.3	Threshold determination for water detection . . . . .	21
4.4	River surface area calculation . . . . .	25
4.5	Data analysis . . . . .	25
<b>5</b>	<b>Results</b>	<b>29</b>
5.1	Image selection . . . . .	29
5.2	Time series of raw data . . . . .	30
5.3	Outlier detection and trend fitting . . . . .	34
5.4	Sensitivity analysis on thresholding . . . . .	38
5.5	River area vs Discharge . . . . .	47
5.6	Correlations. . . . .	48
<b>6</b>	<b>Discussion</b>	<b>51</b>
<b>7</b>	<b>Conclusions and Recommendations</b>	<b>53</b>
7.1	Conclusions. . . . .	53
7.2	Recommendations . . . . .	54
<b>A</b>	<b>Hydrodynamics</b>	<b>57</b>
	<b>Bibliography</b>	<b>61</b>



# NOMENCLATURE

## ABBREVIATIONS

- **EO** Earth Observation
- **ESA** European Space Agency
- **GEE** Google Earth Engine
- **GRDC** Global Runoff Datacenter
- **GRWL** Global River Width from Landsat
- **L5,L7,L8** Landsat 5, 7, 8
- **MNDWI** Modified Normalized Difference Water Index
- **MS** Multi Spectral
- **NDSI** Normalized Difference Snow Index
- **NDWI** Normalized Difference Water Index
- **NIR** Near Infrared
- **RADAR** Radio Detection and Ranging
- **RGB** Red Green Blue
- **RS** Remote Sensing
- **S1, S2** Sentinel-1, Sentinel-2
- **SAR** Synthetic Aperture Radar
- **SWIR** Short Wave Infrared
- **SWOT** Surface Water and Ocean Topography
- **TIRS** Thermal Infrared Sensor
- **TOA** Top of Atmosphere
- **VI** Vegetation Index



# 1

## INTRODUCTION

### 1.1. CONTEXT

#### 1.1.1. THE ROLE OF RIVERS

Rivers play an important role in the water cycle. Not only do they transport water, sediment and ice downstream, they are also very important for transportation, freshwater supply and they play an important role in local ecology [Karpatne et al. \(2016\)](#). Understanding the river dynamics is very important to be able to make use of all river functions and most importantly to protect ourselves against floods. Following [Grimaldi et al. \(2018\)](#), from all the natural disasters worldwide floods are almost the most frequent and disastrous. Numerical models are used to make flood forecasts.

### 1.2. PROBLEM DEFINITION

To be able to make accurate predictions with the hydrodynamic models it is important to have a good estimate of the river geometry and additional information about roughness coefficients, initial water discharge, initial water height and boundary conditions. River conditions such as water flow and water level can be measured in-situ with, for example, gauge measurement stations. Gauge stations have a very high temporal resolution, but a very low spatial resolution. As mentioned in [Gleason and Smith \(2014\)](#), in most countries it is not common to have a large network of well working gauge stations. Even in the countries which have a good network of gauge stations, the network is often still not dense enough.

The problem with obtaining river geometry is, it is very impractical to measure the river geometry, especially when it is needed for a very long reach of the river. One way to get information about river cross-sectional profiles is to do bathymetric surveys. In [Harada and Li \(2018\)](#) it is stated that field surveys of the river channel geometry can take a lot of time, cost a lot of money and are constrained by a lot of logistics. This would cause problems for achieving a sufficient spatial-temporal resolution. Not only acquiring data about the river bathymetry has its problems, also obtaining an accurate river mask has its problems. Rivers are constantly changing, so data should be obtained on a regular basis for both the planform as the bathymetry. After every flood season new measurements are needed, because during the floods most changes in bathymetry take place.

Next to in-situ measurements, remote sensing can be used to observe water dynamics as explained by [Huang et al. \(2018\)](#). Remote sensing has a high spatial-temporal resolution compared to in-situ measurements. On the other hand in-situ measuring is often more accurate than remote sensing. When using remote sensing there are lots of different sensors available, which all come with their own benefits and challenges. For example radar needs lots of processing to deal with noise, but they are not limited by clouds, whereas optical sensors are troubled by clouds but produce less noise.

### 1.2.1. RESEARCH DONE

Within Deltares a project was started named the EO-river project, where EO is short for Earth Observation. The aim of the project is to develop a tool which combines different sources of satellite data as input for their hydrodynamic models. A draft version of the method is shown in Figure 1.1. As part of this project [Thissen \(2019\)](#) developed a method to derive the geometry of the river, which includes the mask and the centerline, based on multispectral images from the Landsat 8 and Sentinel-2 missions. This method to derive the geometry solves the problem of the clouds using a history composite of multispectral images to cover the part of the river which is covered with clouds. This history composite is based on some Google Earth Engine scripts to calculate water occurrence, developed by [Donchyts \(2018\)](#).

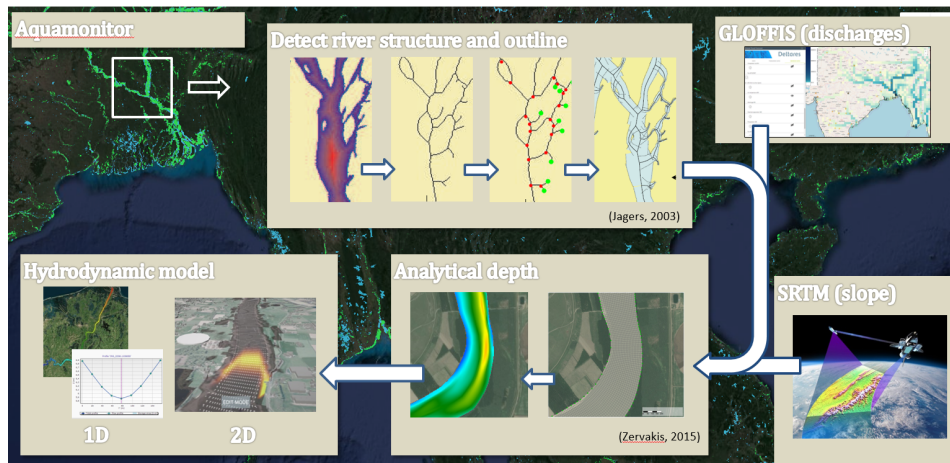


Figure 1.1: The EO-river project developed by Deltares to make use of satellite data as input for hydrodynamic models. The most important input variables are the river structure, the water flow, the longitudinal slope and the analytical depth. This data can potentially be derived from satellite data, but still a lot of research had to be done before this can be implemented as a real working model.

Compared to in-situ measurements remote sensing is more efficient because it has the ability to continuously monitor the Earth surface at multiple scales. Two categories of sensors which are most used to measure the surface water are optical and microwave sensors. Radars send out microwave signals which have very long wavelengths and therefore are able to penetrate through clouds. Furthermore the radar sensors are independent of solar radiation, so they can operate during day and night. Already in 1984 [Bhavsar \(1984\)](#) published the usage of optical remote sensing in hydrology and water management. After him many other studies have been done and especially in the last couple of years the amount of articles published about remote sensing and surface water have more than doubled. Some of the most important papers for this thesis are [McFeeters \(1996\)](#) and [Hanqiu \(2006\)](#), who came up with the 'normalized difference water index' (NDWI) and 'modified normalized difference water index' (MNDWI) for detecting surface water. Furthermore [Schumann and Moller \(2015\)](#) published a review in which he concluded that synthetic aperture radar (SAR) is the most suitable microwave sensor for monitoring flood inundation. Following [Schumann and Moller \(2015\)](#) there are relatively few investigations on the influence of polarization and incidence angle for mapping flooded surfaces, even though they are very important.

### 1.3. RESEARCH OBJECTIVE AND QUESTIONS

A solution for getting a higher spatial-temporal resolution of satellite images concerning water detection can be found in combining different sources of satellite data. A lot of research has been done in combining optical with microwave images, but a good working model still has to be achieved. The aim of this thesis project is to combine microwave and optical satellite sources in a region where optical data is scarce during the rain season, to see if the microwave sensors can fill the gap of the optical sensors. To reach this goal the main question needs to be answered, which is supported by sub questions.

*"How can satellite based optical and microwave images be combined to get a realistic estimation of river geometry to improve hydrodynamic modelling?"*

- Which available satellite data can be used to get geometric information of a river?
- How can different sources of satellite based remote sensing be combined in one hydrodynamic model?
- What is the spatial-temporal resolution when combining optical satellite images with microwave satellites images?
- How are river geometry and discharge related?
- Which validation data is available?

This research is useful because river geometry measurements are scarce, expensive and time consuming when derived from in-situ (bathymetric) surveying. Allen *et al.* (2018) stated, "making satellite data available within a recently proposed less than 2-day time period will make the data potentially useful for flood mitigation and other water management applications". The revisit time of most satellites is multiple days to a month, which is not enough according to Allen *et al.* (2018). But when different satellites can be combined into one method, the time between consecutive images will decrease. If satellite data is proved useful as input for river geometry this can save time and money in hydrodynamic modelling. Furthermore flood forecasts might become more reliable, because larger areas can be covered, which is good for safety measures.

### 1.4. THESIS OUTLINE

The structure of the remainder of the thesis is as follows:

- Chapter 2 provides background information about related work that encompasses the thesis scope and implementation. The main topics in this chapter are the river definition, 1D hydrodynamic modelling, remote sensing, surface water detection and image processing.
- Chapter 3 informs about the Irrawaddy river, including data availability and seasonality in discharge. The Irrawaddy river is used as a case study location for the remainder of the thesis.
- Chapter 4 covers the methodology which is used in the thesis. This step-by-step approach starts with image selection, followed by resampling of the images, water detection, thresholding, outlier detection and seasonal trend fit.
- Chapter 5 shows the results for every step of the methodology.
- Chapter 6 provides a discussion, which contains a reflection on the thesis and the attribution of the results to the knowledge of the research area.
- Chapter 7 contains conclusions and recommendations. In this chapter the research questions are answered and recommendations for use and for future research are given.

Additionally, one appendix is supplemented to this thesis. Appendix A contains information about hydrodynamics, which plays an important role in hydrodynamic modelling.



# 2

## BACKGROUND

In this chapter some background information about rivers, hydrodynamic modelling, remote sensing, surface water detection and image processing is discussed. Someone with basic knowledge about these subjects can skip this chapter. All acronyms that are used in this thesis are summarised in the nomenclature.

### 2.1. RIVER DEFINITION

In this section it is explained which role rivers play in the water cycle and how we can distinguish between different types of rivers. To get a better understanding of the river dynamics, which includes the flow and shape of the river, in Appendix A information is added about hydrodynamics. This information is not directly used for the method in this thesis, but shows that there are many variables which influence river behaviour. For most variables assumptions can be made, but for more accurate predictions, the monitoring of these variables is very important.

On land, most fresh water accessible to humans can be found in lakes, rivers, soil and groundwater. Rivers are part of the water cycle, because they can transport water and ice, see Figure 2.1. The water cycle is in balance when the amount of water entering and leaving the system is equal. Following [Sichangi \*et al.\* \(2016\)](#), knowledge about the water cycle is necessary for flood management, climate studies, and water resource management. Next to the transport function of the rivers, they are also very important for transportation, freshwater supply and supporting local ecology.

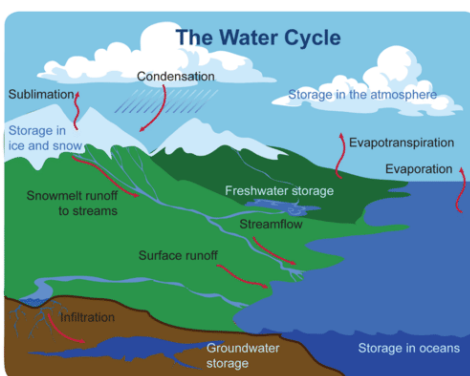


Figure 2.1: The water cycle ([LibreTexts, 2018](#)).

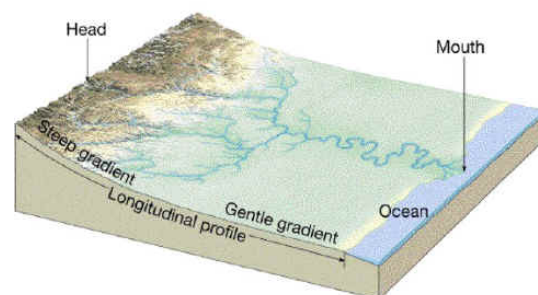


Figure 2.2: Typical concave upward longitudinal profile of a river.

Typical rivers have a concave upward longitudinal profile, as shown in Figure 2.2. This means that the bed elevation decreases in the downstream direction linearly with downstream distance. Furthermore both grain-size and bed slope decrease in downstream direction. A river can be divided in a upper, lower and middle reach based on among others the above mentioned characteristics. In the upper reaches there are mountains

which cause a steep gradient resulting in high flow velocities. As water from tributaries enters the river, its discharge increases in downstream direction. This results in an increasing river width and depth towards the lower reaches of the river. In the lower reaches of the river often a delta or estuary is formed as a passage to the sea and this region becomes influenced by tides and sea-level fluctuations. In the different regimes, rivers can have different kinds of channel patterns, such as braided, meandering, anabranching and straight. Most rivers carry a range of sediment sizes, from large rocks to very fine clay. In the upper regime the river bed is usually coarse, while further downstream the sediment becomes much finer due to sorting and abrasion.

## 2.2. 1D HYDRODYNAMIC MODELLING

The purpose of 1D hydrodynamic modelling is to make the complex flow situation in the river to a simple one-dimensional stream tube. This is done by using the basic flow equations as explained in Appendix A.0.2 and making some assumptions about the input parameters which are not directly available. This simplified model can then be used to make water level predictions. The hydrodynamic model calculates water level and flow velocity for each cross-section or node. Furthermore the model covers 1D equations for 'point features' such as weirs, bridges and sluices. In Figure 2.3 an example of a simplified 1D channel is shown, with spatial evenly distributed cross-sections. The cross-sections are 'in-bank', but they might also be extended to cover the floodplain. The cross-sections are always perpendicular to the main flow. The floodplain can also be represented with reservoir units (flood cells), see Figure 2.4.

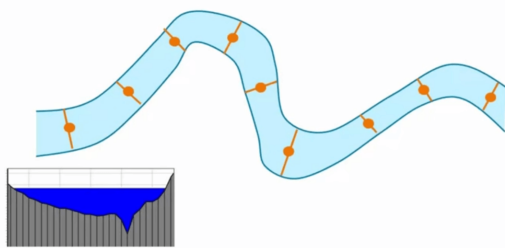


Figure 2.3: Example of a simplified 1D channel with equally spaced cross-sections, which can be used in 1D hydrodynamic modelling.

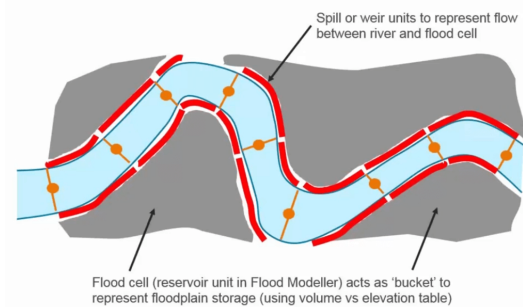


Figure 2.4: Example of a simplified 1D channel with floodplains represented by flood cells.

Following Grimaldi *et al.* (2018) the models can broadly use two different methods to come to a hydraulic flood forecast. They can either provide a full solution of the shallow water equation or they can use a simplified approximation. In the simplified approximations some terms of the conservation equation can be neglected.

### 2.2.1. DATA REQUIREMENTS

The data requirements of a 1D hydrodynamic model:

- River network: channel centerlines, flow direction data, a river mask and cross-sections which give information about depth and river shape.
- Dimensions of point features such as bridges/weirs/sluices (if present).
- Topography for flood plain (Grid data).
- Linear features (for example, roads) and other things that could affect flow routes.
- Channel and floodplain roughness (based on standard values and than calibrate).
- Boundary conditions (usually upstream inflow and downstream water levels with sometimes additional lateral inflows and extractions).
- Initial conditions (usually the floodplain is dry, and the river has a flow and water level).
- Runtime data: start/finish time and timesteps.
- Calibration data (observations): water levels, flood maps etc..
- Numerical grid.

## 2.3. REMOTE SENSING

Remote sensing is a collective term for all measuring techniques that gain knowledge about an object without directly touching it. These techniques can be subdivided in active and passive remote sensing, see Figure 2.5. An active technique sends out electromagnetic waves and measures the return signal. A passive sensor only measures (part of) the electromagnetic spectrum emitted or reflected by an object. Remote sensing can take place from different platforms such as, ships, aeroplanes, drones, air-balloons, satellites and more. In the scope of this thesis, the focus will mainly be on spaceborn remote sensing techniques, because satellites have an almost global coverage with new data available every day to every month, depending on the orbit of the satellite. There are commercial and freely available satellite images and because the commercial data comes with high costs, only freely available data is used for this thesis. All satellites have different sensors which measure at different wavelengths, furthermore some satellites have a high orbit which results in a high sampling frequency, but low resolution and some have it the other way around. The resolution of the images is also dependent on the quality of the sensors.

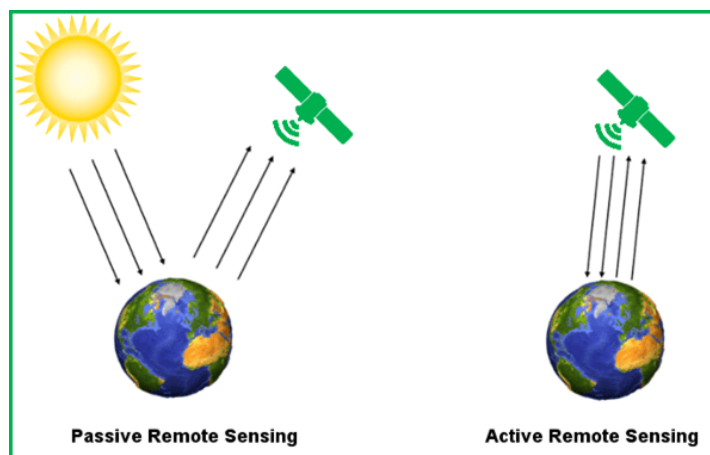


Figure 2.5: The difference between active and passive remote sensing. Passive remote sensing instruments measure only the radiation emitted by the object being viewed or reflected by the object from another source than the instrument, which is mostly sunlight. Active remote sensors provide their own source of radiation and measure the returning signal.

### 2.3.1. MULTISPECTRAL SENSORS ON BOARD OF LANDSAT, SENTINEL, MODIS AND ASTER

Multispectral satellites measure electromagnetic radiation in different wavelengths. Some examples of satellites containing multispectral sensors are the Landsat, Sentinel, MODIS and ASTER missions. In Figure 2.6 it is shown that not all Landsat satellites are operational anymore. Only Landsat 7 and Landsat 8 are still in operation, nevertheless Landsat 7 got a failure in 2003 resulting in images with missing data. Landsat 9 is planned to be launched in December 2020. In Figure 2.7 an overview is given of the bands used by the above mentioned satellites. In this thesis only the optical bands from the multispectral images are used. Those optical bands include the visible 'red', 'green' and 'blue' band and furthermore the optical bands include the near infrared and the short wave infrared bands. In the Table 2.1 the most important characteristics of all satellites are summarised.

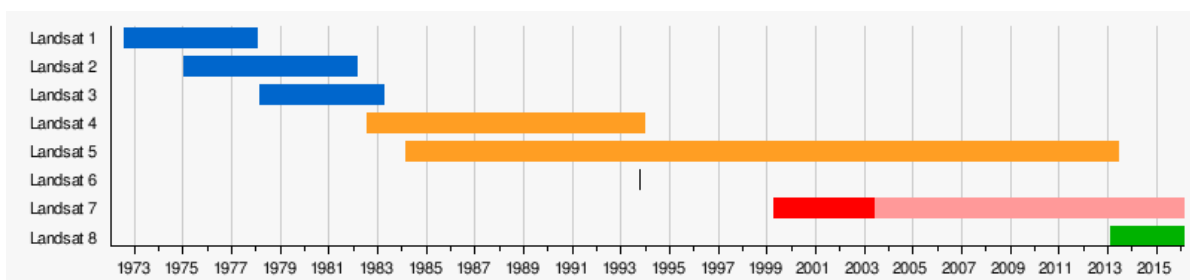


Figure 2.6: Landsat time span, [Wikipedia \(2019a\)](#).

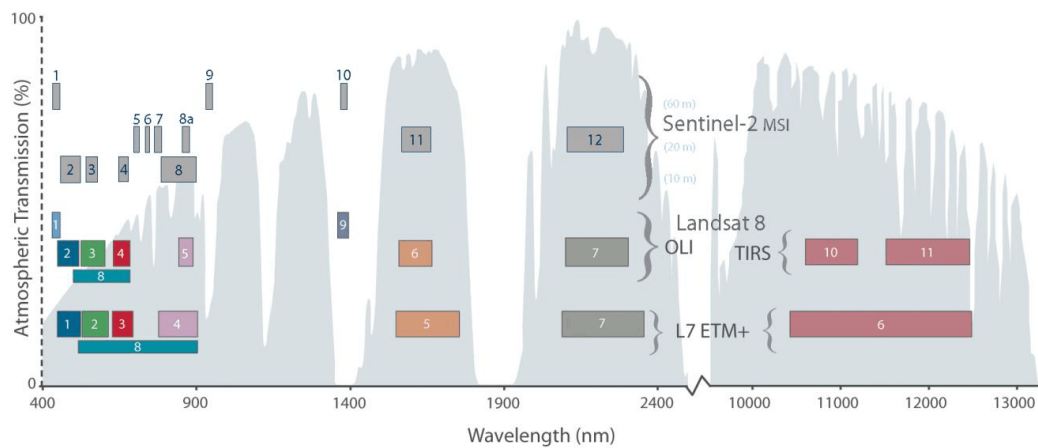


Figure 2.7: Comparison of Landsat 7, 8 Sentinel 2, ASTER and MODIS bands [USGS](#).

### 2.3.2. MICROWAVE SENSOR ON BOARD OF SENTINEL-1

The Sentinel-1 mission is part of the Copernicus program of the European Commission in partnership with the European Space Agency (ESA). The mission consists of two satellites (Sentinel-1A and Sentinel-1B) which are 180 degrees from each other in a polar orbit around the Earth. The satellites measure with Synthetic Aperture Radar (SAR) at the C-band (5,405 GHz), this wavelength makes it possible to make images of the Earth surface without weather influence. Furthermore the active remote sensing makes it possible to measure during the night, because it is not dependent on solar radiation. The Sentinel-1 satellites were launched in April 2014 and April 2016 and are still operational. The satellites have a 12-day repeat cycle, but because they are used together the repeat cycle becomes 6 days.

The C-band imager can operate in three modes with various observation strategies, swath width, and spatial resolution. Over land mostly the interferometric wide-swath mode (IW) is used, which has a fine resolution of 5mx20m with a swath width of 250km. Furthermore there is the Extra Wide Swath mode (EW), which is used to acquire data over a wider area of 400 km swath at 20mx40m spatial resolution. The EW mode is mostly used for monitoring of the sea-ice, polar zones and certain maritime areas. [ESA](#)

Next to different swath modes, there are different polarisation modes in which Sentinel-1 can operate. The instrument has one transmitter, which can switch between horizontal (H) and vertical (V) polarisation. Two parallel receive chains are built in for the 'H' and 'V' polarisation. The different transmission and reception can be combined to four different acquisition modes, namely the single 'VV' and 'HH', and the dual polarisation 'HH+HV' and 'VV+VH' products. [Hardy et al. \(2019\)](#) found that open water and low-backscattering areas are best to distinct in VV polarisation. On the other hand [Vachon and Wolfe \(2011\)](#) states that 'HH' polarization usually performs better in separating land from water under calm water conditions. The scattering of open water shows less scattering with the 'HH' polarization compared to the 'HV' or 'VV' polarization and is less sensitive to capillary waves created from wind.

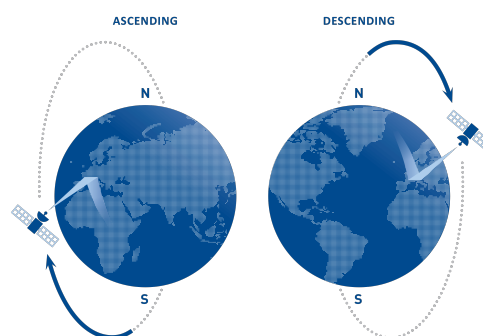


Figure 2.8: Ascending and descending orbit example from [TRE](#).

All SAR satellites travel from the north pole towards the south pole for half of their trajectory and this direction is called the descending orbit. When the satellite is travelling from the south towards the north pole, this is called an ascending orbit. The same area is revisited along both orbits. As shown in Figure 2.8 the satellite will look from another direction between the two orbits.

### 2.3.3. OVERVIEW SATELLITES

All above mentioned satellites are summarised in Table 2.1. This table gives a better understanding on how every satellite is designed as a compromise between availability and resolution, and how they all measure in different bands.

Mission	Multispectral					SAR
	Landsat 7	Landsat 8	Sentinel-2A&B	ASTER	MODIS (Terra & Aqua)	Sentinel-1A&B
Availability	~16 days	~16 days	~5 days	~16 days	~0.5 days	~6 days
Resolution	30m - VNIR & SWIR 15m - PAN 100m - TIR	30m - VNIR & SWIR 15m - PAN 100m - TIR	10m	15m - VNIR 30m - SWIR 90m - TIR	250-1000m	5x20m
Launch Date	April 15, 1999	February 11, 2013	June, 2015	December 18, 1999	Terra: December 18, 1999 Aqua: May 4, 2002	S-1A: April 2014 S-1B: April 2016
Nr of Bands	8	11	13	14	36	C-band (5,05 GHz)

Table 2.1: Overview of some satellites with multispectral and SAR sensors from which images are made freely available by ESA or NASA.

### 2.3.4. CHALLENGES WHEN USING SATELLITE DATA

A problem can occur when using images taken with Landsat 7. This mission shows some failure resulting in stripes of missing data, called the SLC failure. When the missing data is (partly) occurring over the cross-section this can result in a lower river width than actually is the case, see Figure 2.9. Another problem that can occur is that the satellite image only covers part of the cross-section. This can also result in a too low estimate of the river width, see Figure 2.10.

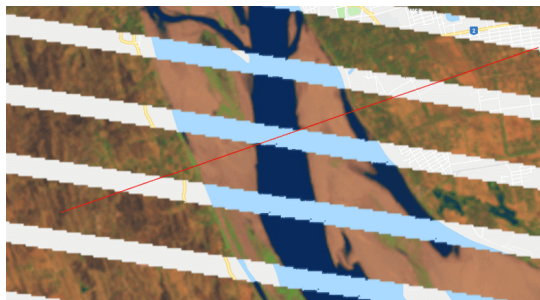


Figure 2.9: Cross-section at the Magway station at 14-03-2007. Due to failure of the Landsat 7 mission part of the river cross-section is not taken into account.



Figure 2.10: Cross-section at the Magway station at 23-03-2007. The satellite image only covers part of the cross-section, resulting in a too low estimate of river width.

Every remote sensing mission has its advantages and disadvantages. On one hand, natural phenomena can cause problems. To start with, false positive detection of water can be observed in areas with shadows due to topographic conditions or the presence of clouds. On the other hand satellite images present human-made processes, such as infrastructure and agriculture. Another problem is caused by satellite data latency as mentioned by Allen *et al.* (2018). Satellite data latency refers to the time period between when a satellite makes an observation and when that information is available to the user in an actionable format. Multiple technological factors contribute to the latency of satellite products including the time necessary to acquire, store, downlink, process, and distribute the data. Hence, trade-offs exist between satellite data latency and data quality, such that longer latency products are more internally consistent and of higher quality.

### 2.3.5. GLOBAL PRODUCTS

Some products are generated making use of satellite data to give information about the earth surface. Some of these global products give information about river related values. It is important to know which global products exist, because they can be of use for this thesis.

#### GLOBAL SURFACE WATER EXPLORER

The 'Global Surface Water Explorer' is a freely available dataset that maps the location and temporal distribution of water surfaces at the global scale over a period of 32 years (1984-2015) and provides statistics on the extent and change of those water surfaces. The dataset is produced from coarse-spatial-resolution satellite observations, higher-resolution seasonality maps have been produced using Landsat 5, 7 and 8 multitemporal orthorectified satellite imagery at 5- to 10-year intervals. All Landsat images over multiple decades have been used to map seasonality and changes at continental and sub-continental scales. The 'Global Surface Water Explorer' dataset is freely available from <https://global-surface-water.appspot.com/> and more information can be found in [Pekel \*et al.\* \(2016\)](#). This dataset can be used to get an indication of the river history that can be used for the case study. It shows if there are long term changes and or seasonal changes that have to be taken into account.

#### GRDC GLOBAL RUNOFF DATA CENTRE

To exchange hydrological data and information on a global scale, the Global Runoff Data Centre (GRDC) became operational. The GRDC dataset contains river discharge data from more than 9500 stations from 161 countries, which are plotted in Figure 2.11. For every station the monthly/yearly minimum, maximum and mean discharge statistics are available. Primarily, This data is provided by National Hydro-logical and Hydro-Meteorological Services. The data is available for research programmes and projects from researchers, universities and other organisations. ([GRDC, 2019](#))

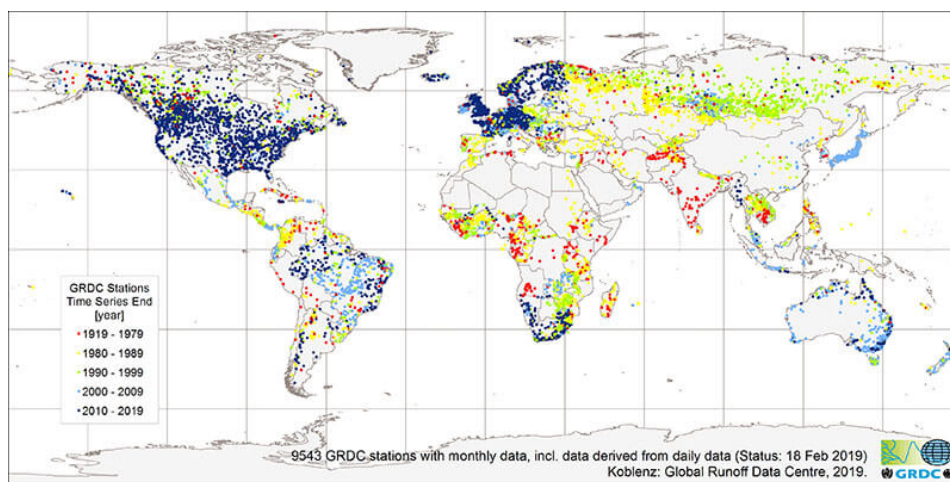


Figure 2.11: GRDC stations with monthly data, indicated by time series end. ([GRDC, 2019](#))

#### GRWL GLOBAL RIVER WIDTHS FROM LANDSAT

[Allen and Pavelsky \(2018\)](#) built the Global River Widths from Landsat (GRWL) database to characterize the global coverage of rivers and streams. The GRWL is a global compilation of river planform geometry at a constant-frequency discharge. From gauge station measurements, the months were determined when that river was near mean discharge. During this months Landsat scenes were captured. The GRWL contains only rivers of more than 30m wide at mean annual discharge. [Allen \*et al.\* \(2018\)](#) found that GRWL width data was most accurate and complete at widths wider than 90 m (about three Landsat pixels).

### SWOT MISSION

A future mission to keep in mind is the Surface Water and Ocean Topography (SWOT) mission that is designed to survey the Earth's surface water, observe the fine details of the ocean's topography, and measure how water bodies change over time on a global scale. The launch is targeted for September 2021. SWOT is anticipated to be able to observe river conditions night and day, and during cloudy weather conditions. (Biancamaria *et al.*, 2016)

### GOOGLE EARTH ENGINE

The Google Earth Engine (GEE) is a free planetary-scale platform from Google which can be used to download, process and analyse Earth science data from all over the world. The public data archive includes more than forty years of historical imagery and scientific datasets, which are updated and expanded daily. The GEE has its own web-based IDE from the Earth Engine JavaScript API. The code editor is designed to make developing complex workflows fast and easy. In this thesis the GEE is used as main source for the satellite data and the platform is used to do most of the processing and analysing of the data.

## 2.4. SURFACE WATER DETECTION

Water has specific characteristics which makes it differ from its surroundings. By making use of this characteristics both microwave images and multispectral images can be used to detect water. In this section both the method using microwave images and the method using multispectral images to detect water are explained.

### 2.4.1. SURFACE WATER DETECTION USING MULTISPECTRAL IMAGES

Vegetation Indices (VI) are used for the gathering of ecological information from satellite and drone data through the analysis of multi- or hyper-spectral imagery bands. The reflectance of light changes with variation in chlorophyll content, plant type, sugar content, water content and other factors as shown in Figure 2.12. The indices are very useful in separating classes of interest. The main spectral bands that are relevant to the application of VI's are given in Table 2.2.

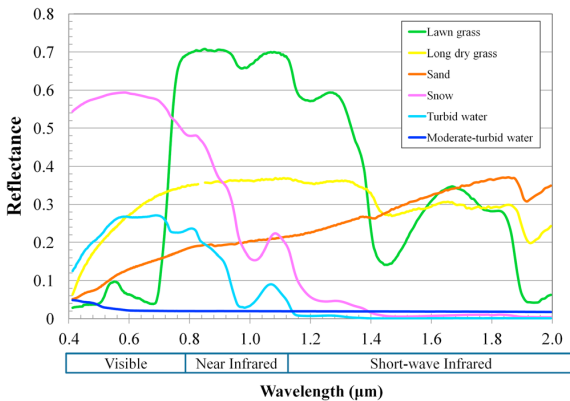


Figure 2.12: Typical spectral signatures of bare soil, green vegetation and water in the shortwave spectral region, collected from United States Geological Survey (USGS) digital spectral library.

Visible light	
Blue	450-495 nm
Green	495-570 nm
Red	620-750 nm
Infrared	
Near Infrared (NIR)	750-900 nm
Short Wave Infrared1 (SWIR)	900-3000 nm
Thermal Infrared (TIR)	3000-14000 nm

Table 2.2: Different bands in the electromagnetic spectrum that are used to calculate vegetation indices.

McFeeters (1996) was one of the first to use the Normalized Difference Water Index (NDWI) to detect clear water. The NDWI (Eq. 2.1) makes use of the fact that water easily absorbs radiation at the near-infrared wavelengths and less in the shorter green region of the spectrum.

$$NDWI = \frac{\rho_{green} - \rho_{nir}}{\rho_{green} + \rho_{nir}} \quad (2.1)$$

In Eq. 2.1  $\rho_{green}$  stands for the reflectance in the green band and  $\rho_{nir}$  for the reflectance in the NIR band. The index is dimensionless and values vary between -1 and 1, where a value greater than zero mostly indicates

water. Next to the NDWI other spectral indices have been used for water detection. For example, the Modified Normalized Difference Water Index (MNDWI) from Hanqiu (2006) appears to be more sensitive, due to the use of the shortwave infrared band instead of the near-infrared band used in NDWI. The infrared bands are shown in Figure 2.13.

$$MNDWI = \frac{\rho_{green} - \rho_{swir1}}{\rho_{green} + \rho_{swir1}} \quad (2.2)$$

In Eq. 2.2  $\rho_{green}$  stands for the reflectance in the green band and  $\rho_{swir1}$  stands for the reflectance in the SWIR1 bands which ranges from 1570-1650nm for the Landsat 8 satellite and from 1613-1610nm for the Sentinel-2 satellite. The MNDWI is sensitive to snow and ice, since it makes use of the short-wave infrared band, which is also used to separate snow from clouds with the Normalized Difference Snow Index (NDSI). A problem with the MNDWI is that it can not separate snow from water. Donchyts (2018) shows that a good separation between water and snow/ice can be achieved by using the near-infrared band instead of the short-wave infrared band, which is less sensitive to snow/ice content. In fact, substituting the short-wave infrared band for the near-infrared band results in the NDWI. In Huang *et al.* (2018) it is stated that the MNDWI is more reliable than NDWI (if there is no snow), because the SWIR band is less sensitive to concentrations of sediment and other optical active constituents in the water, compared to the NIR band.

The above mentioned indices (NDWI and MDNWI) are probably the most used indices for water detection, nevertheless other spectral indices have been investigated in the last years. In Fisher *et al.* (2016) seven water index methods for classifying water in 30m resolution Landsat imagery were tested. The accuracy of each index was highly dependent on the composition of the validation pixels, there was no index performing best across all water and non-water pixel types. All indexes and thresholds were found to perform consistently across images from the Landsat sensors.

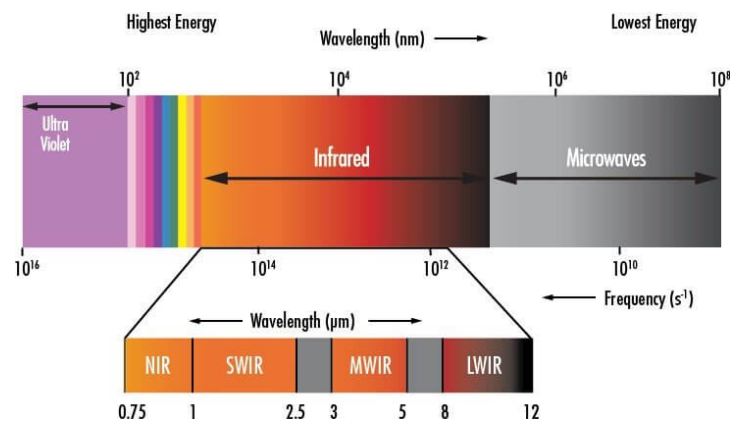


Figure 2.13: The short wave infrared region (SWIR) of the electromagnetic spectrum.

#### 2.4.2. SURFACE WATER DETECTION USING SENTINEL-1 IMAGES

In contrast to multispectral images, where NDWI or MNDWI is used to detect surface water, in Donchyts (2018) a method is explained to detect surface water with Sentinel-1 images. Objects on the ground have distinctive polarisation signatures, reflecting different polarisations with different intensities. Water surfaces are generally smooth and result in a low back-scatter of radar wavelengths. The surrounding terrain is assumed to be rough and cause more diffuse scattering with moderate backscatter. This principle is shown in Figure 2.14. Thresholding can be used to make a distinction between water and dry land. Following Solbø (2005) the threshold depends on the contrast between the land and the water classes and has to be set for each Sentinel-1 scene. Factors that influence this contrast are the polarisation and incidence angle of the SAR system. Furthermore wind or wave can induce ripples on the water surface, which increases the backscattering. To diminish the effects of speckle noise in Sentinel-1 images, a new speckle filter was implemented within the Google Earth Engine, based on Perona and Malik (1990), to improve the quality of images and to decrease the number of spurious sharp edges not belonging to surface water.

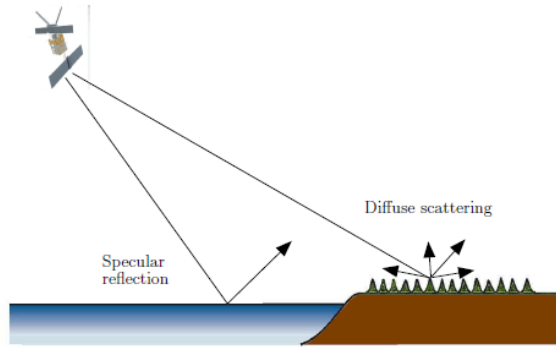


Figure 2.14: Scattering mechanisms of water bodies and dry land in non-forested areas Solbo (2005).

### 2.4.3. OTSU THRESHOLDING

It was suggested by Ji and Wylie (2009) to use a flexible threshold over time or spatial over the image, to get better results in water detection. Otsu thresholding can be used to automatically divide image pixels in two or more classes. For example a greyscale or other single band image can be reduced to a binary image. This method originates from Otsu (1975). Assuming that the histogram of all values of the image is a bivariate distribution, a threshold can be selected that minimizes the intra-class (or within class) variance:

$$\sigma_b^2(t) = w_0(t)w_1(t)(\mu_0(t) - \mu_1(t)), \quad (2.3)$$

where  $t$  is the threshold,  $w_0$  and  $w_1$  are the probabilities of each class and  $\mu_0$  and  $\mu_1$  are the mean values of each class. Donchyts (2018) made an algorithm in the Google Earth Engine that can calculate the Otsu threshold in a efficient way by using the following formula from Otsu (1975):

$$t = \underset{t}{\operatorname{argmax}}(\sigma_b^2(t)). \quad (2.4)$$

## 2.5. IMAGE PROCESSING

### 2.5.1. BICUBIC RESAMPLING OF IMAGES

Images can be resampled to improve the resolution of the image. Different interpolation techniques can be used to resample images, such as bilinear and nearest-neighbour interpolation. Keys (1981) was the first to come with the new technique of bicubic interpolation for digital image processing. Bicubic interpolation gives smoother results than other interpolation techniques, but is more time consuming. Bilinear interpolation only takes into account 4 pixels (2x2), whereas bicubic interpolation uses 16 pixels (4x4).

The basic idea of cubic interpolation is to estimate the values between any two points as a cubic function. Following Keys (1981), for equally spaced data, many interpolation functions can be written in the form:

$$g(x) = \sum_k c_k u\left(\frac{x - x_k}{h}\right). \quad (2.5)$$

In this equation  $h$  is the sampling increment,  $x_k$  are the interpolation nodes,  $u$  is the interpolation kernel and  $g(x)$  is the interpolation kernel. The  $c_k$ 's are parameters which depend on the sampled data. Examples of the interpolation kernels ( $u$ ) are given in Figure 2.15.

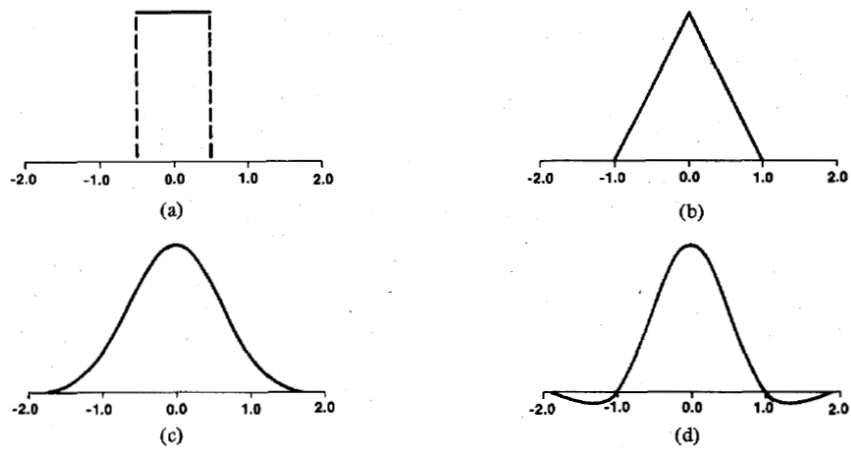


Figure 2.15: Examples of interpolation kernels from [Keys \(1981\)](#).

### 2.5.2. CANNY EDGE DETECTOR

The Canny Edge Detector can be used to find locations in the image which represent certain features, such as water-land boundaries. These edges can be used to mask the river and for example calculate the area of the river mask. The original Edge Detection algorithm originates from [Canny \(1986\)](#). The Canny edge detection algorithm can be broken down in 5 different steps:

1. If the image is RGB or other multi band, convert the image to greyscale or other single band property.
2. Smooth the image with a Gaussian filter to remove some noise.
3. Find the intensity gradients of the image.
4. Thin out the edges by applying a non-maximum suppression.
5. Determine potential edges by double thresholding.
6. Suppress all edges that are weak and not connected to other (strong) edges.

An example of performing these five steps is given in Figure 2.16.

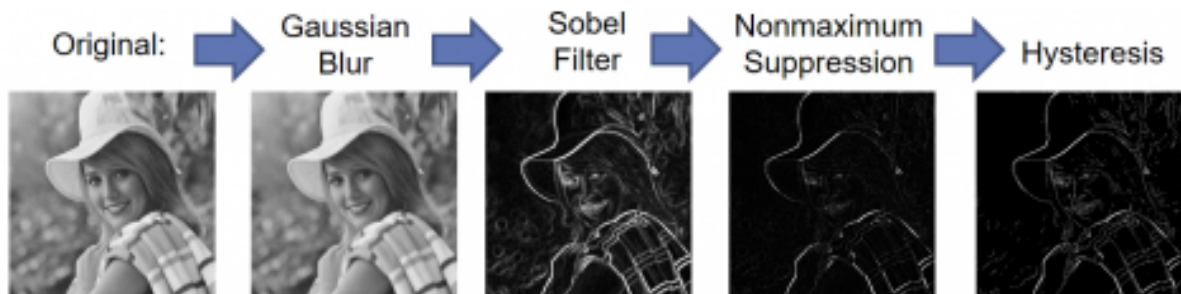


Figure 2.16: Example of the five steps used for edge detection [Ringwald \(2012\)](#).

# 3

## THE IRRAWADDY RIVER

In this thesis the Irrawaddy river is used as case study location because this river shows a lot of seasonal variation in discharge and geometry. In this chapter some background information about the river is given, which includes information about the river, the data availability and the seasonality in discharge.

### 3.1. LOCATION AND BACKGROUND

Two locations along the Irrawaddy river were used for this case study. These locations are Sagaing, which is close to Mandalay, and Katha. At both locations historical discharge data from the GRDC database is available. Mandalay is a city located in the middle of Myanmar, see Figure 3.1. Katha is the first city upstream of Mandalay which has a GRDC data point. Both locations are in the middle reach of the river and show a braiding character. The Irrawaddy river is the most important river of Myanmar and also one of the biggest rivers in Southeast-Asia with a length of 2.210 km.



Figure 3.1: Location of Mandalay along the Irrawaddy River in Myanmar.

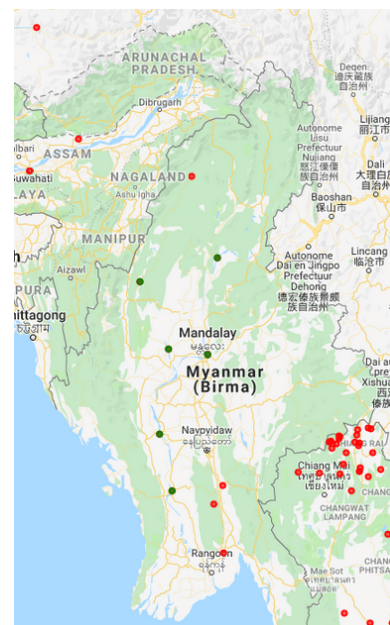


Figure 3.2: GRDC stations in Myanmar (green). From north to south: Katha, Mawlaik, Monywa, Sagaing, Magway and Pyay.

### 3.2. DATA AVAILABILITY

#### 3.2.1. SATELLITE DATA

To get a feeling how often satellite images from the Sentinel and Landsat missions are available over the Irrawaddy river, in Figure 3.4 the amount of clear images and in Figure 3.3 the total amount of images available each year are plotted for each different satellite. The image is clear, when there are no clouds over the region of interest. The Sentinel-1 images are not filtered on cloud cover because they are not influenced by the clouds. In 1996 only Landsat 5 was available, in 1999 Landsat 7 was launched and years later also Landsat 8 and Sentinel-2 were launched and Landsat 5 is no longer in operation. Landsat 9 is planned towards a launch in December 2020 and will have the same properties as Landsat 8 with some improvements.

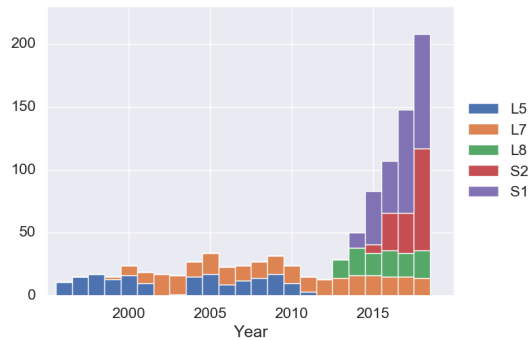


Figure 3.3: Amount of satellite images covering Sagaing available each year.

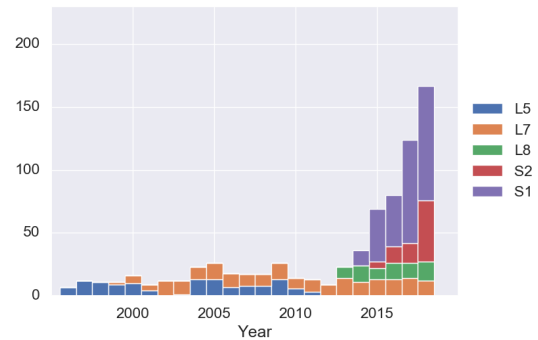


Figure 3.4: Amount of 'clear' satellite images covering Sagaing available each year.

In Figure 3.5 a rugplot is made for the Sagaing region which shows all the available multispectral images from Landsat 8 and Sentinel-2 over the entire year 2018. The green stripes indicate the 'clear' images and the red stripes the images that contain too many clouds. When this rugplot is made for other years when both Landsat 8 and Sentinel-2 are operational, the same pattern is visible. During the months June until October there is a rain season and most images will contain too many clouds to be useful for estimating river geometry.

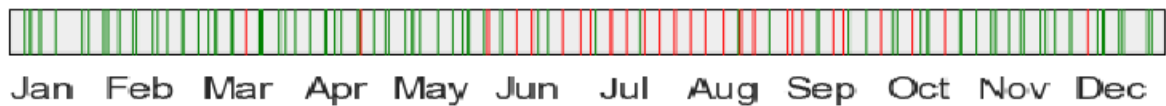


Figure 3.5: Rugplot of available clear (green) and not clear (red) images that cover Sagaing taken by Landsat 8 and Sentinel-2 in 2018. This year a total of 106 images are available from which 78 are clear enough to use.

In Figure 3.6 a rugplot is made for the Sagaing region which shows all available Sentinel-1 images over the year 2018. It is clear that over the entire year the Sentinel-1 images are useful. A total of 91 images are taken in 2018.

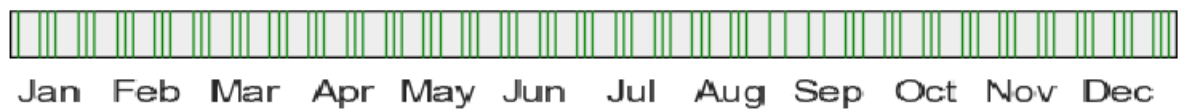


Figure 3.6: Rugplot of available images that cover Sagaing taken by Sentinel 1 in 2018. This year a total of 91 images are available.

### 3.2.2. GRDC DISCHARGE DATA

Daily discharge data from four stations along the Irrawaddy River and two along the Chindwin River can be requested from the GRDC database. Those stations are coloured green in Figure 3.2. For every station a time series is available of daily discharge data from 01-01-1996 until 31-12-2010, only for Sagaing a longer period from 01-01-1978 until 31-12-2015 is available. The six stations are listed below, but only the Katha and Sagaing timeseries were used.

- Irrawaddy River - Pyay
- Irrawaddy River - Magway
- Irrawaddy River - Sagaing
- Irrawaddy River - Katha
- Chindwin River - Monywa
- Chindwin River - Mawlaik

From the GRDC discharge data histograms can be plotted containing all measurements from the available time period. The discharge histogram of Sagaing is given in Figure 3.7 and the discharge histogram of Katha is given in Figure 3.8. The figures show a peak at the lower discharges, because high discharge occurs less frequent during the rain season. Furthermore the discharge at Katha is lower than at Sagaing, which is logical because Katha is upstream from Sagaing and between those locations water is added to the river by side streams.

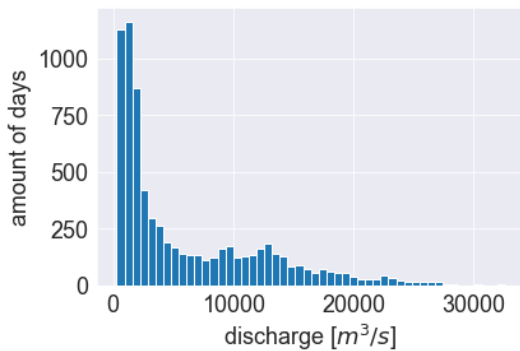


Figure 3.7: Histogram of GRDC discharge data at the Sagaing station.

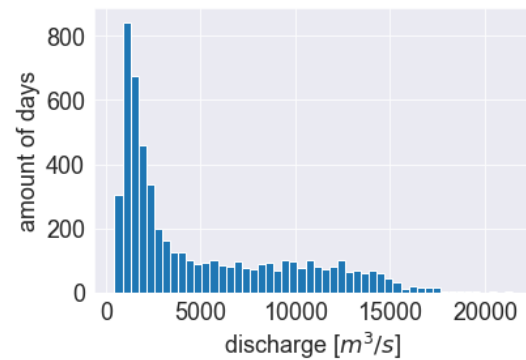


Figure 3.8: Histogram of GRDC discharge data at the Katha station.

The discharge is not constant in time, which is shown in Figure 3.9 and Figure 3.10. Those figures show boxplots of the average and inter-quartile range of the river discharge for every month. Both figures show a peak in discharge during the monsoon (June-October).

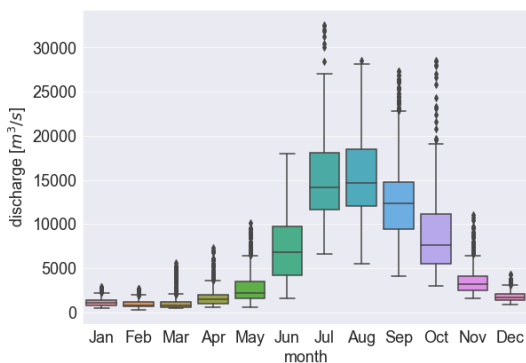


Figure 3.9: Discharge seasonality at Sagaing, calculated with daily GRDC discharge data from 1978 to 2015.

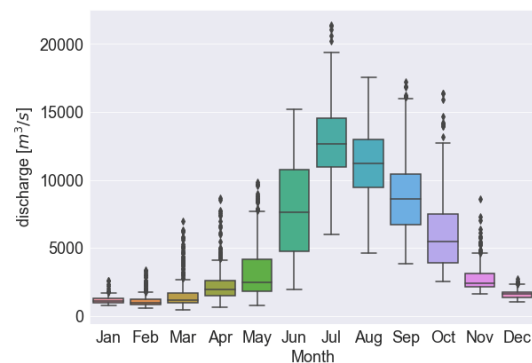


Figure 3.10: Discharge seasonality at Katha, calculated with daily GRDC discharge data from 1996 to 2010.

In Figure 3.11 and 3.12 the average and inter-quartile range for every year from 1996 to 2015 at Sagaing and from 1996 to 2010 at Katha are plotted. The figures show that in some years the average discharge is higher than during other years. Furthermore some years have higher peak discharges than other years. In general both location show the same variations.

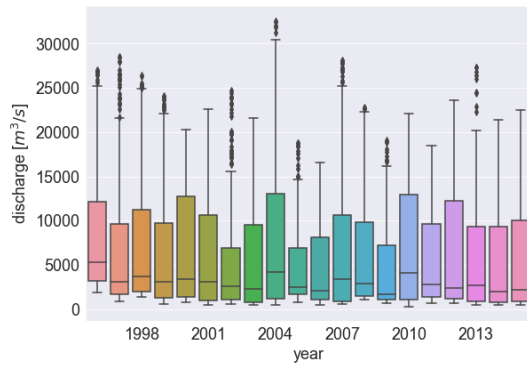


Figure 3.11: Discharge seasonality at Sagaing, calculated with daily GRDC discharge data from 1996 to 2015.

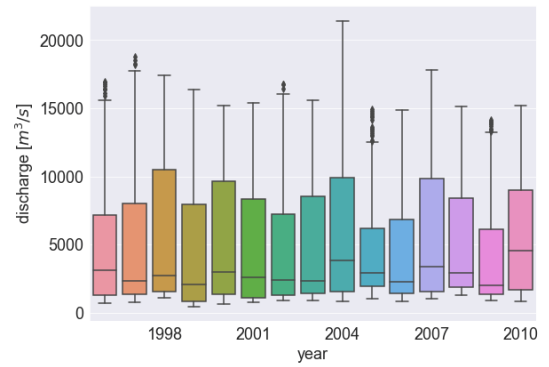


Figure 3.12: Discharge seasonality at Katha, calculated with daily GRDC discharge data from 1996 to 2010.

# 4

## METHODOLOGY

In this chapter the method is derived which is used to investigate whether the combination of microwave and optical remote sensing will improve the existing methods to derive river geometry from satellite data. This step-by-step approach starts with image selection, which is followed by resampling of the images and water detection based on spectral indices or backscatter values. Next the water mask can be derived with the use of some basic thresholding algorithms. This water mask is used to calculate the area of the river within a certain polygon. The area estimations are analysed by looking at the outliers and a (seasonal) trend is extracted.

### 4.1. IMAGE SELECTION

All images were collected with the Google Earth Engine (GEE) and filtered based on the region of interest, satellites and cloud cover. In this section these three steps are explained in more detail.

#### 4.1.1. SATELLITES

The Landsat 7, Landsat 8 and Sentinel-2 missions were used to provide the multispectral images. These missions are sometimes abbreviated with L7, L8 and S2. The source for the microwave images was the Sentinel-1 satellite, abbreviated with S1. In Chapter 2 'Background' some more information is given on how all these satellites work.

#### IMAGE VARIABLES

All images have some variables which change between acquisitions and might influence the results. For the Sentinel-1 images there were some image variables to take into account which included the polarisation and instrument mode. For simplifying it was chosen to select only Sentinel-1 images with a 'VV' polarisation and a 'IW' instrument mode. Furthermore the Sentinel-1 images were taken during both 'ascending' and 'descending' orbits. It was not investigated what the influence is on the results when using another polarisation or instrument mode, nevertheless the influence of the orbit direction was examined.

#### PRE-PROCESSING

When using Sentinel-1 images, several specialised algorithms are necessary to obtain calibrated and orthorectified images to get a homogeneous subset of Sentinel-1 data. This pre-processing was performed in the GEE using the Sentinel-1 toolbox. This toolbox provides three steps of processing: 'thermal noise removal', 'radiometric calibration' and 'terrain correction'. For the multispectral images only the Tier 1 and Real-Time data calibrated for the top-of-atmosphere (TOA) reflectance were used. The calibration coefficients were extracted from the image metadata. More information about TOA computation can be found in [Chander \*et al.\* \(2009\)](#).

### 4.1.2. REGION OF INTEREST

The location used as case study in this thesis is Katha. Another location along the Irrawaddy river in Myanmar is Sagaing and this location could be used as validation. At both locations historic discharge data is available from the GRDC database (GRDC (2019)). To be able to make estimations of the river area, cross-sections and polygons have been drawn by hand at these locations along the river, as shown in Figure 4.1. The polygons include mainly the 2km downstream of both GRDC locations. The city at the right side of the Sagaing polygon in Figure 4.1 is actually the city Mandalay, whereas the city Sagaing is around 10 km downstream of Mandalay, nevertheless the location of the cross-section and polygon are called Sagaing, because that is the name of the GRDC data point.

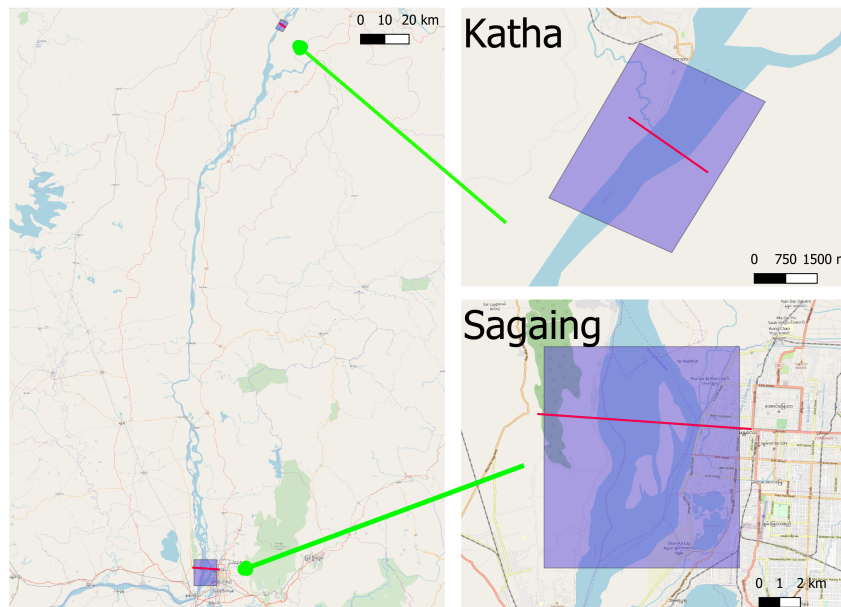


Figure 4.1: Locations of the cross-sections and polygons near Katha and Sagaing located on the Open Street Map.

### 4.1.3. CLOUD COVER

One of the most occurring problems when using multispectral imaging to investigate processes at the earth surface, is cloud coverage. When using multispectral imaging, a cloud can be misclassified as water. To avoid this problem, the images that contain clouds over the region of interest should not be used. A simple method would be to only select images that have a zero percentage of cloud cover. But because the region of interest is very small compared to the entire satellite image, it might be very well possible that even when the cloud cover is higher than zero percent, the clouds do not cover the region of interest. Donchyts (2018) implemented a function in the GEE to filter images based on the historic cloud frequency over the region of interest and this method was used to for this thesis.

## 4.2. RESAMPLING

Image resampling is used to transform a sampled image from one coordinate system to another and to improve the resolution of the image. For the different coordinate systems to match, the discrete image has to be converted into a continuous surface. This 'image reconstruction' can be performed with an interpolation procedure called bicubic resampling. In Chapter 2 more information is given about how bicubic resampling works. After the image is reconstructed it can be easily transformed to every other coordinate system. When the image is upscaled, pixels are added. An example of a resampled image is shown in Figure 4.3, which is the result of resampling Figure 4.2. In this thesis all images were resampled using this bicubic resampling method.

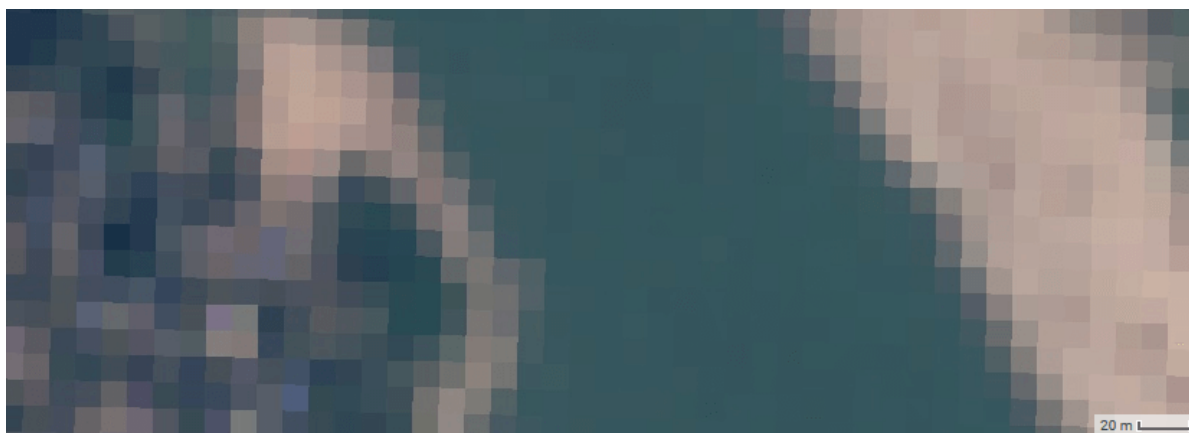


Figure 4.2: Close-up of a Sentinel-2 image, displaying the red, green and blue band over a region around Sagaing. The original pixels are visible, because no resampling is used. Sentinel-2 has a resolution of 10 meter, which corresponds to the size of the pixels in this image.

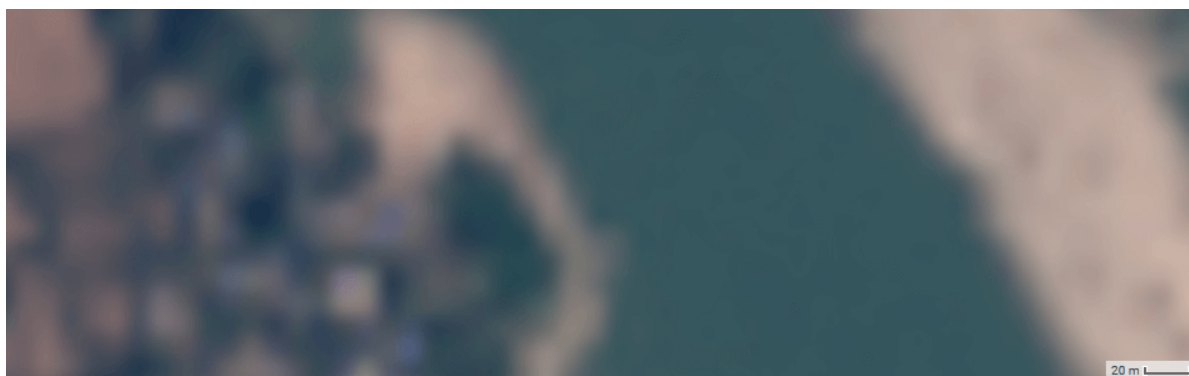


Figure 4.3: Close-up of the same Sentinel-2 image as Figure 4.2, displaying the red, green and blue band over a region around Sagaing, after bicubic resampling was applied.

## 4.3. THRESHOLD DETERMINATION FOR WATER DETECTION

As explained in Chapter 2, water can be detected with multispectral images by calculating the NDWI or MNDWI values, and for microwave images with the use of the backscatter values. The right threshold values are needed to separate non-water pixels from water pixels. In Figure 4.4 an example of the Katha polygon on 16-04-2018 is shown in four different ways, namely the false color image, the NDWI values, the MNDWI values and the SAR backscatter values. The false color, NDWI and MNDWI values are calculated from a Sentinel-2 image and the backscatter is directly from the Sentinel-1 image. From this figures it becomes clear that the river has higher NDWI/MNDWI values than the surrounding areas and for the backscatter it is the other way around, namely the river shows lower backscatter values than the surroundings. To detect the water both fixed thresholding and dynamic thresholding was used and in the end those methods were compared to each other. The dynamic threshold was calculated with the Otsu thresholding algorithm (see Section 4.3.2) and

for the fixed thresholds some values from the literature were used. In Huang *et al.* (2018) it is stated that a threshold of 0 is often applied when using NDWI to detect water and for the MNDWI the threshold is close to 0.2. Panchagnula *et al.* (2012) derived that the threshold is between -6 and -15 dB when using 'VV' polarization to detect water, this range is large because the threshold is depending on wind speed or image viewing geometry. For this thesis a fixed threshold of -15 dB is used for Sentinel-1 images.

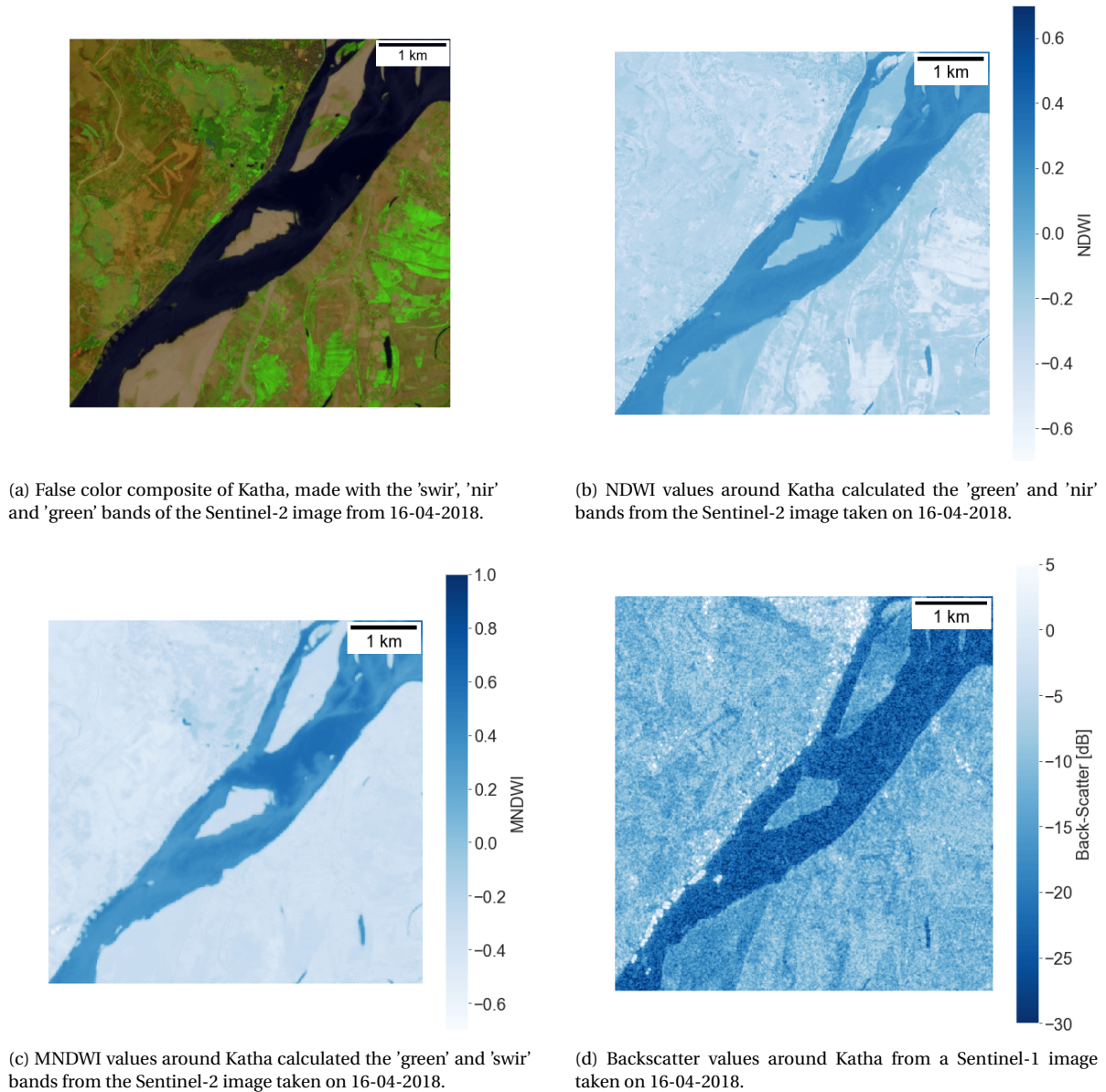


Figure 4.4: The Katha polygon from Figure 4.1 on 16-04-2018, displayed in four different ways; namely showing the (a) false color composition, (b) NDWI values, (c) MNDWI values and (d) backscatter values.

### 4.3.1. CROSS-SECTIONS

To get a feeling on how the values of NDWI, MNDWI and backscatter vary over the cross-sections of the river as shown in Figure 4.1, the cross-section values from the images in Figure 4.4 are plotted in Figure 4.5. The NDWI and MNDWI show a steep gradient at the same locations in the graph, which indicate the boundaries between land and water. The backscatter values also show a gradient at the same locations, only those gradients are more irregular. The threshold value needs to be somewhere on the steep gradients. For this research more cross-sections from different days were compared to see how these values vary. The Katha

cross-section is 2322 meter long and is sampled with 5000 points along this cross-section, so the distance between each point is 0.46 meters. If more detailed investigation would be necessary, the cross-sections could be made with a smaller sampling interval, which would make the graph smoother.

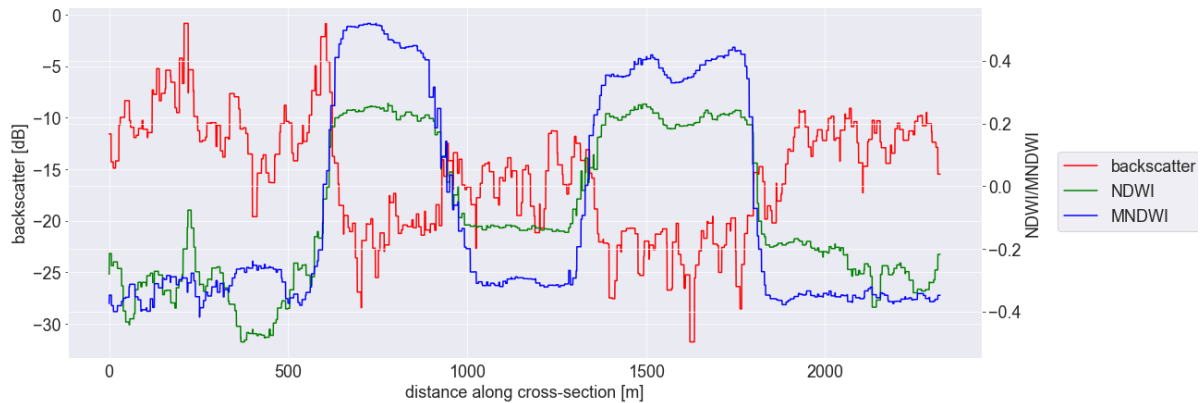


Figure 4.5: NDWI, MNDWI and backscatter values over the cross-section near Katha on 16-04-2018.

### 4.3.2. OTSU THRESHOLDING

Otsu thresholding is an algorithm that returns a single or multiple intensity thresholds to separate pixels into two or more classes. The method searches for the thresholds that minimise the intra-class variance. An explanation on how Otsu thresholding works is given in Chapter 2. In this section both the single Otsu thresholding and the multiple Otsu thresholding methods are discussed. The methods are applied to the images from Figure 4.4 and the results are shown in Figure 4.10.

#### SINGLE OTSU THRESHOLDING

The single Otsu thresholding algorithm has some limitations. The method works best when the histogram has a clear bimodal distribution with a sharp valley between the two peaks. When the object, for example the river, is small compared to the background the distribution is no longer bimodal, because the 'land' pixels dominate the histogram with a very high peak.

For most programming languages algorithms exist to calculate the Otsu threshold. For the single Otsu thresholding in the GEE the algorithm as implemented by [Donchyts \(2018\)](#) was used with the variables as shown in Table 4.1. The effect of using slightly other values was not investigated in this thesis.

	<b>cannyThreshold</b>	<b>cannySigma</b>	<b>minValue</b>
<b>NDWI</b>	0.6	0.2	-0.2
<b>MNDWI</b>	0.6	0.2	-0.2
<b>SAR</b>	9	4	-20

Table 4.1: Values used for the variables 'cannyThreshold', 'cannySigma' and 'minValue' functions for calculating single Otsu threshold values in the Google Earth Engine.

#### MULTI OTSU THRESHOLDING

When the image contains more than two classes, shown by multiple peaks in the histogram, multi Otsu thresholding can be used. Multi Otsu thresholding works the same as Otsu thresholding for a normal distribution, but returns multiple threshold values, separating the different classes. For this thesis only the single Otsu thresholding was used to estimate threshold values, because most histograms showed a bimodal distribution.

### 4.3.3. CANNY EDGE DETECTION AND OTSU THRESHOLDING COMBINED

The Canny Edge detector and the Otsu thresholding can be combined to find a threshold value for detecting water. More information about the Canny Edge detector is given in Chapter 2. To start with, the Canny Edge detector was used to find the locations in the image where there is a high gradient in one of the image bands or a self defined bands such as NDWI/MNDWI or backscatter. At the locations with a high gradient a buffer of 30 meters was applied to the the edge to take into account the surrounding pixel values. The result of applying the Edge Detector to the NDWI image in Figure 4.4, is given in Figure 4.6. From all pixels within this buffered edge a histogram was made and from this histogram the threshold can be calculated using single Otsu thresholding, see Figure 4.8.

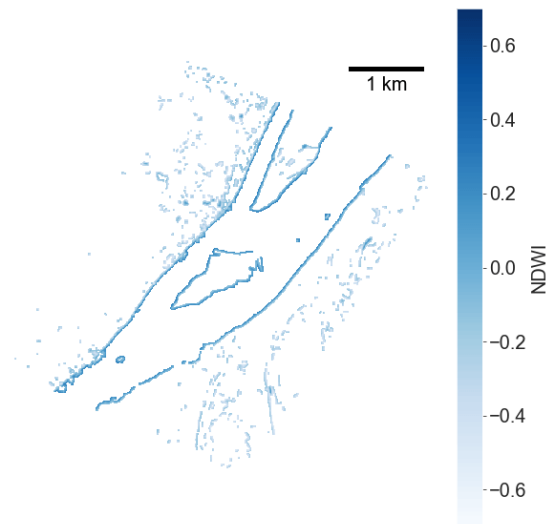


Figure 4.6: Edges selected from figure 4.4 with the Canny Edge detector.

In the figures below histograms of NDWI values from the Sentinel-2 image on 16-04-2018 from Figure 4.4 are shown when using all pixels in the Katha polygon (Figure 4.7) and when using the Canny Edge detector (Figure 4.8). For both the Otsu threshold is calculated in the GEE and for the histogram containing all pixels this results in -0.0347, and when using only the edges this is -0.0043. The histogram containing all pixels shows a small peak between -0.2 and -0.1, whereas the canny edge histogram shows a bimodal distribution. For this thesis all Otsu thresholds were calculated using the histograms after applying the Canny Edge detector.

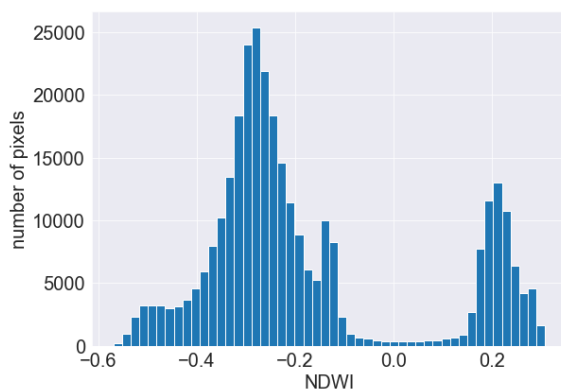


Figure 4.7: Histogram showing the NDWI values from all pixels in the Sentinel-2 image from Figure 4.4. The Otsu threshold calculated from this histogram is -0.0347.

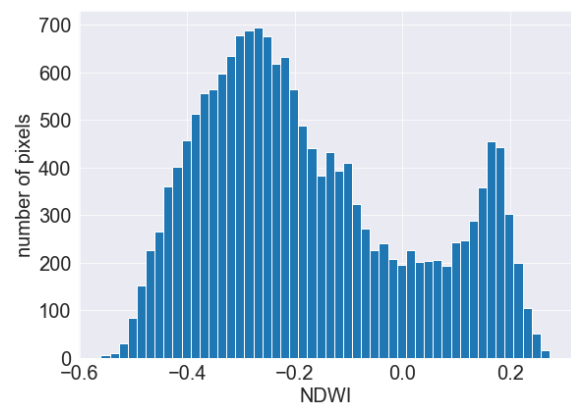


Figure 4.8: Histogram showing the NDWI values from all pixels within the edges calculated with the Canny Edge detector in the Sentinel-2 image from Figure 4.4. The Otsu threshold calculated from this histogram is -0.0043.

#### 4.4. RIVER SURFACE AREA CALCULATION

To be able to compare the water detection based on optical images with the results from the microwave images, for both methods not the river geometry, but the area of the river within the polygon was calculated. When both methods result in similar area calculations, the methods could be combined. The area calculation was performed as follows. After the image selection, for the multispectral images the NDWI was calculated and for the Sentinel-1 images no further calculations had to be performed to get the backscatter. This NDWI and backscatter images were divided in water and non-water pixels by either using the fixed threshold from Section 4.3 or the dynamic Otsu thresholding from Section 4.3.3. As a next step the river area was calculated by counting all water pixels within the polygon from Figure 4.1.

#### 4.5. DATA ANALYSIS

For the river surface area, time series have been made for the different sources of satellite data and for using a dynamic or fixed threshold. The (seasonal) trend was estimated and outlier detection could be done. Both the method for the seasonal trend fit and the outlier removal are explained in this section.

##### SEASONAL TREND FIT

The seasonal trend fit was performed in Python using the package 'statsmodel.tsa.seasonal'. With this package the data can be split into a level, trend, seasonality and noise with the following formula of an additive model, where  $y(t)$  represents the time series data:

$$y(t) = Level + Trend + Seasonality + Noise \quad (4.1)$$

An example of this additive model is given in Figure 4.9. The additive model was chosen, because it was assumed that the time series of the estimated areas would show a linear trend with a linear seasonality with constant frequency and amplitude. Before this function could be applied the data had to be resampled to a one day interval, because the satellite images were available on an irregular basis. Linear interpolation was used to calculate the area for days that no satellite data was available.

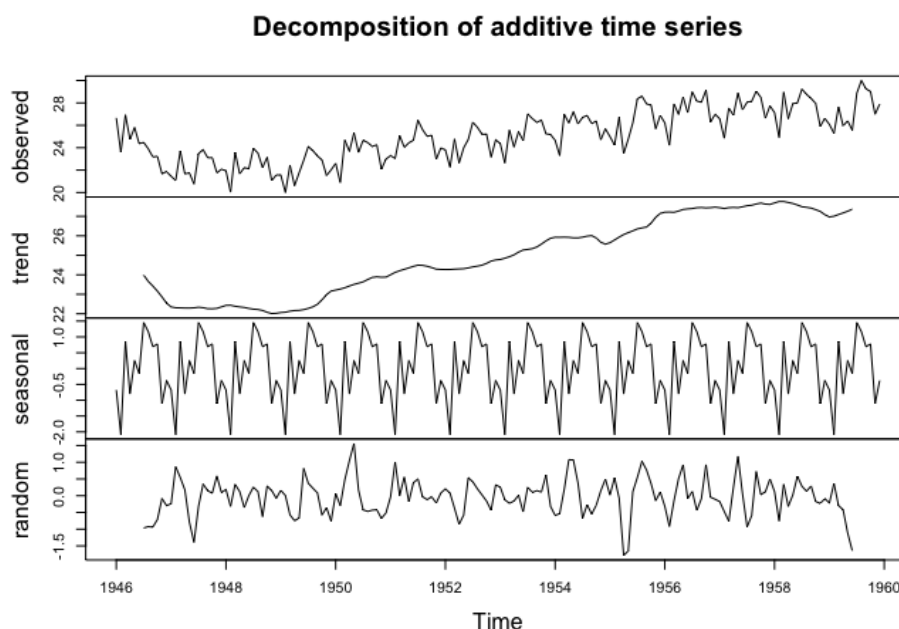


Figure 4.9: Example of additive time series, split into a trend, seasonality and noise component. [Astaraky](#)

## OUTLIER REMOVAL

After the seasonal trend was fitted, the data points that showed large deviation from this trend were examined by looking at the original images to see what caused the exceptionally high or low water area estimations. When the original images showed that the data point was indeed an outlier, this point could be manually removed from the dataset.

### 4.5.1. VALIDATION

After the data was cleaned from outliers, the (seasonal) trend was calculated and a sensitivity analysis was performed on how sensitive the method is on varying the threshold. As a next step some joint distribution functions were plotted to correlate the different sources of satellite images to each other and to investigate the effects of using a fixed threshold or dynamic Otsu thresholding.

At last the area estimations are compared to discharge data from the GRDC dataset at the Katha region. This discharge data is only available from 1996 until 2010 for the Katha station. Even though only Landsat 8, Sentinel-2 and Sentinel-1 images were used to calculate the river area, Landsat 7 and Landsat 5 were used to calculate the river areas in the period from 1996 until 2010, because the other satellites were not yet operational during this period.

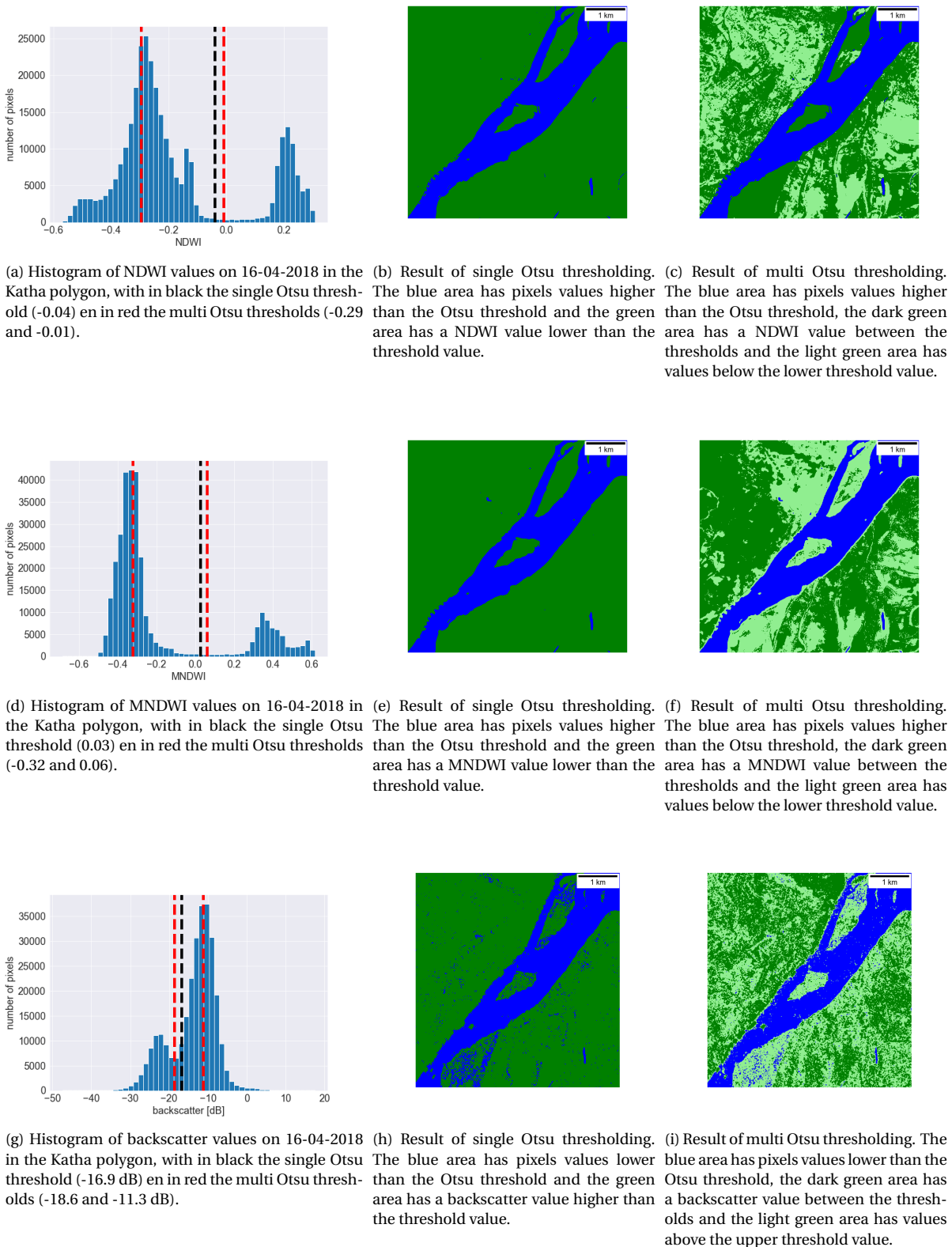


Figure 4.10: Example of the difference between single and multi Otsu thresholding on the image around Katha on 16-04-2018 for the NDWI, MNDWI and backscatter. For the original images see Figure 4.4.



# 5

## RESULTS

In this chapter, the method as discussed in Chapter 4 is applied and the results are interpreted and evaluated. A summary is given about the image selection. This summary gives information about the amount of images and the revisit periods of the different satellite missions. Furthermore time series are plotted which show the estimates areas calculated from the different satellite missions in the Katha region. The first time series shows the result when using fixed thresholds and the next time series shows the results when Otsu thresholding is used. Also a time series of the Otsu thresholds is showed and a sensitivity analysis is performed on the influence on the area estimations when varying the threshold value. Next the most striking outliers are discussed and outliers are removed from the dataset. Furthermore, joint distribution plots show the relations between the different satellites, the different thresholds options and different indices for the multispectral images. Finally, the relation between river area and river discharge is investigated.

### 5.1. IMAGE SELECTION

After the image selection has taken place, as explained in Chapter 4, in Table 5.1 the revisit periods for the different satellites and combinations of all satellites are summarised. The results show that the Sentinel-1 images have a shorter revisit period compared to the multispectral satellites. Nevertheless the combination of Landsat 8, Sentinel-2 and Sentinel-1 images results in the shortest average revisit period, averaged over a whole year. During the monsoon Sentinel-1 images can be used, whereas there are no 'clear' multispectral images available. If the monsoon is not taken into account the average revisit period for the Landsat 8 and Sentinel-2 satellites would be around 10 days, instead of 14 days. The revisit period of 0 days for the Landsat 8, Sentinel-2 combination is caused by the fact that both satellites can pass during the same day.

	<b>Min revisit period</b>	<b>Max revisit period</b>	<b>Average revisit period</b>	<b>Total amount of images 2014-2019</b>
<b>L8 &amp; S2</b>	0	176	14 days	136
<b>S1</b>	2	21	7 days	201
<b>All</b>	0	21	5 days	337

Table 5.1: Overview of minimum, maximum and average revisit period for the multispectral satellites (Landsat 8 & Sentinel-2), Sentinel-1 satellite and the combination of the three.

## 5.2. TIME SERIES OF RAW DATA

### 5.2.1. SURFACE AREA TIME SERIES WITH FIXED THRESHOLD

In Figure 5.1 the river area estimations in the Katha polygon are plotted based on the 'clear' images from Landsat 8, Sentinel-2 and Sentinel-1 in the period 2014-2019. The area estimations from the multispectral satellites are based on the NDWI values and a fixed threshold of 0. The area estimations from Sentinel-1 are based on a fixed threshold of -15 dB. Figure 5.1 shows that all satellites follow a seasonal trend conform to the seasonal variation in discharge as shown in Figure 3.10. During the months June until October there is a monsoon, which causes high discharges which results in a larger river area than during the lower discharges. Even though a trend is visible, the spread in the measurements is large, especially during the monsoon when there are some very high area estimations and some much lower area estimations in the same time period. The estimations from the Sentinel-1 images show the most variation. Furthermore the time series show that the density of the measurements is higher in the winter months and lower during the monsoon, when almost no multispectral images are available due to the clouds. The frequency of Sentinel-1 images is constant over the year.

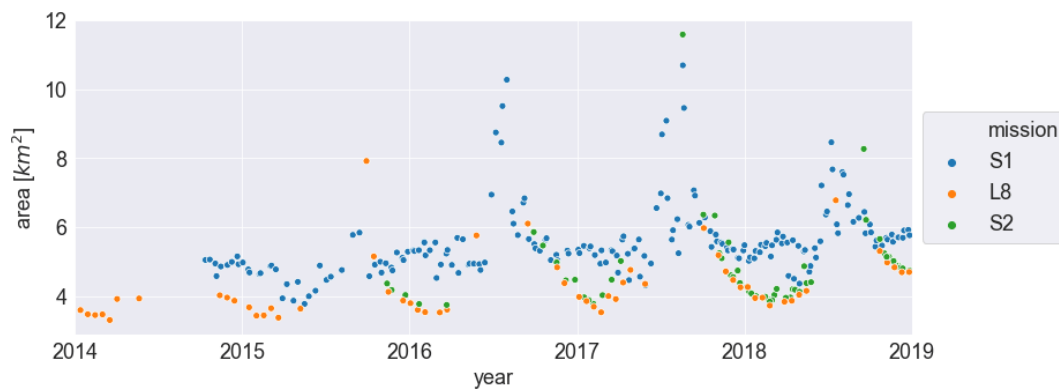


Figure 5.1: Time series of area estimations in the Katha polygon from 2014-2019 when a fixed NDWI threshold of 0 is used for the multispectral images from Landsat 8 and Sentinel-2, and -15 dB for the backscatter values from Sentinel-1.

From the time series in Figure 5.1 boxplots are made showing the average and inter-quartile range of estimated river area for every month. Figure 5.2 shows the monthly boxplot for the Landsat 8 and Sentinel-2 images and Figure 5.3 shows the boxplot of area estimations from Sentinel-1 images. Both figures show that during the monsoon the river area is larger than during the other months. The difference between the figures is that the estimations based on the Sentinel-1 images show a dip in area estimation in the month May before the area increases during the monsoon. The reason for this is still unclear.

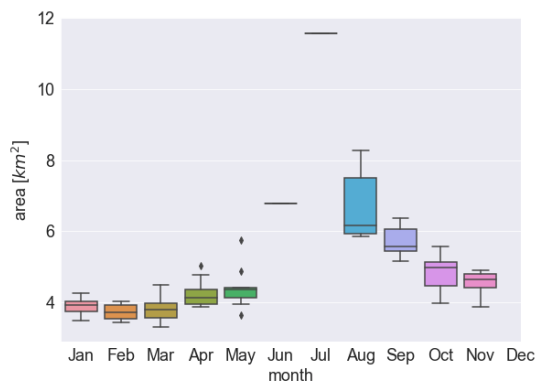


Figure 5.2: Boxplot showing the average and inter-quartile range of monthly area estimations based on the NDWI values from multispectral images from Landsat 8 and Sentinel-2, using a fixed NDWI threshold of 0.

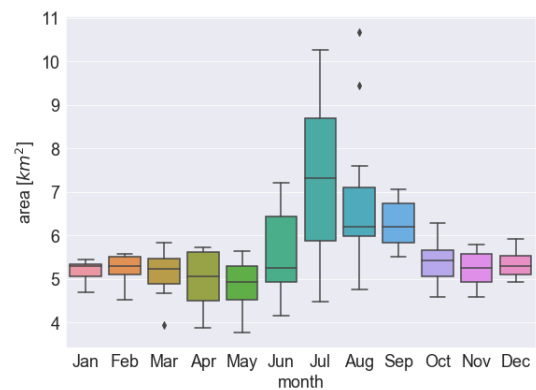


Figure 5.3: Boxplot showing the average and inter-quartile range of monthly area estimations based on the backscatter values from SAR images from Sentinel-1, using a fixed backscatter threshold of -15 dB.

From the time series in Figure 5.1 boxplots were made showing the average and inter-quartile range of estimated river area for every year from 2014 until 2018. Figure 5.4 shows the yearly boxplot for the Landsat 8 and Sentinel-2 images and Figure 5.5 shows the boxplot of yearly area estimations based on Sentinel-1 images. Both figures show that the area of the river within the Katha polygon has increased in the period from 2014 until 2018. This can be the result of increasing discharge or river geometry changes.

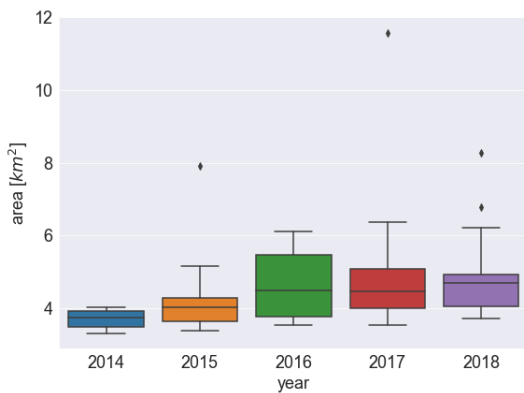


Figure 5.4: Boxplot showing the average and inter-quartile range of yearly area estimations based on the NDWI values from multispectral images from Landsat 8 and Sentinel-2, using a fixed NDWI threshold of 0.

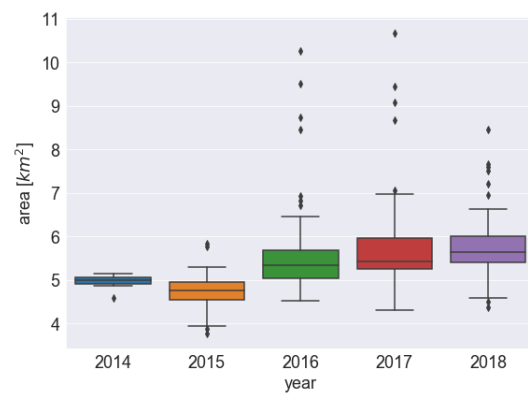


Figure 5.5: Boxplot showing the average and inter-quartile range of yearly area estimations based on the backscatter values from SAR images from Sentinel-1, using a fixed backscatter threshold of -15 dB.

### 5.2.2. AREA TIME SERIES WITH DYNAMIC THRESHOLD

In Figure 5.6 the river area estimations in the Katha polygon are plotted based on the 'clear' images from Landsat 8, Sentinel-2 and Sentinel-1 during the period 2014-2019. The area estimations from the multispectral satellites are based on the NDWI values and the area estimations from the Sentinel-1 satellite are based on backscatter values. To calculate the area the Canny Edge detector and dynamic Otsu thresholding have been used as explained in Chapter 4. A time series of the thresholds which have been used are shown in Figure 5.11 for the multispectral images and in Figure 5.12 for the Sentinel-1 images. The same as in Figure 5.1, with the fixed thresholds, Figure 5.6 also clearly shows a seasonal trend and a lack of data for the multispectral images during the monsoon months. Compared to the time series based on a fixed threshold, there are less extreme area estimations. Nevertheless the area estimations based on Sentinel-1 constantly show higher values than the area estimations based on the multispectral images.

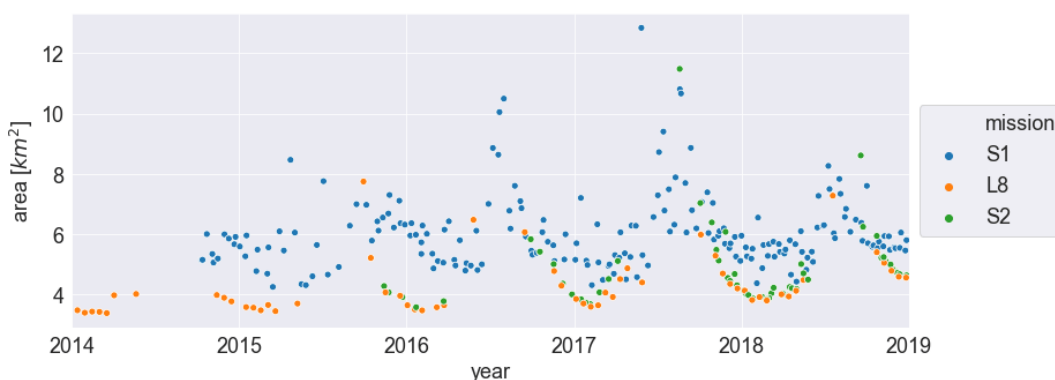


Figure 5.6: Time series of area estimations in the Katha geometry from 2014-2019 when Otsu thresholding is used for both the NDWI from Landsat 8 and Sentinel-2, and the backscatter values from Sentinel-1.

From the time series in Figure 5.6 boxplots are made showing the average and inter-quartile range of estimated river area for every month when Otsu thresholding was used. Figure 5.7 shows the monthly boxplot for the Landsat 8 and Sentinel-2 images and Figure 5.8 shows the boxplot of area estimations with Sentinel-1 images. The same as in the boxplots using a fixed threshold (5.4 and 5.5) a seasonal trend is visible of higher area estimations during the monsoon. The only difference when using Otsu thresholding instead of fixed thresholding is that in the boxplot in Figure 5.8 there is not the small dip that is visible in Figure 5.5.

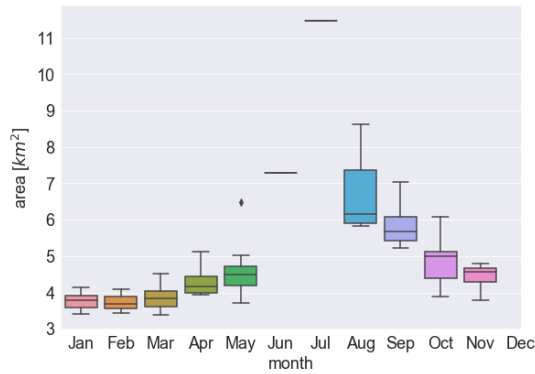


Figure 5.7: Boxplot showing the average and inter-quartile range of monthly area estimations based on the NDWI values from multispectral images from Landsat 8 and Sentinel-2, using Otsu thresholding.

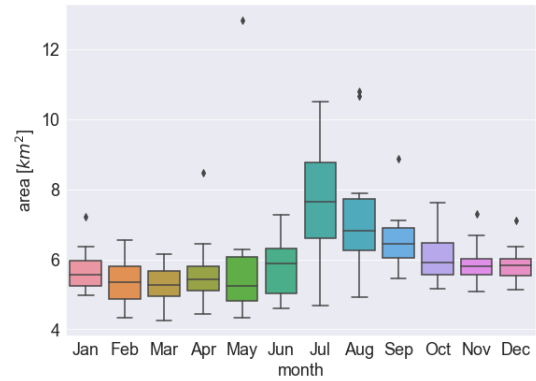


Figure 5.8: Boxplot showing the average and inter-quartile range of monthly area estimations based on the backscatter values from Sentinel-1 images, using Otsu thresholding.

From the time series in Figure 5.6 boxplots were made showing the average and inter-quartile range of estimated river area for every year from 2014 until 2018. Figure 5.9 shows the yearly boxplot for the Landsat 8 and Sentinel-2 images and Figure 5.10 shows the boxplot of yearly area estimations based on Sentinel-1 images. Figure 5.9 show that the area of the river within the Katha polygon has increased in the period from 2014 until 2018, which can be the result of increasing discharge or river geometry changes. On the contrary, Figure 5.10 shows that the area estimations of the river are more or less constant.

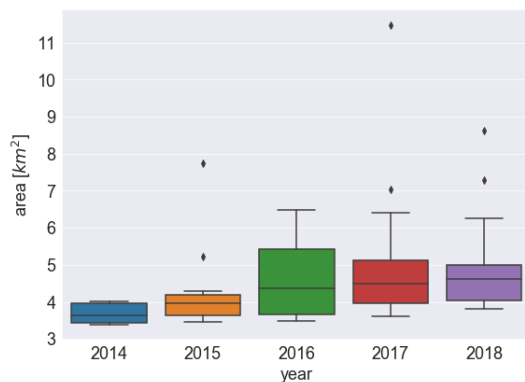


Figure 5.9: Boxplot showing the average and inter-quartile range of yearly area estimations based on the NDWI values from multispectral images from Landsat 8 and Sentinel-2, using Otsu thresholding.

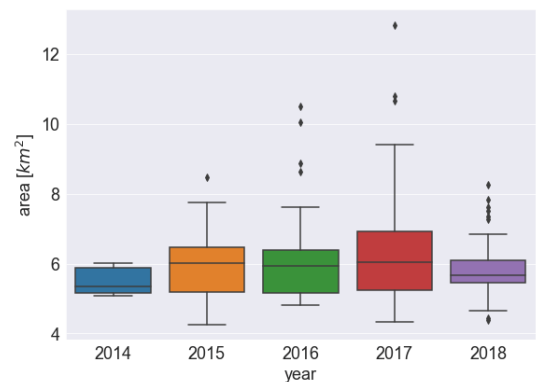


Figure 5.10: Boxplot showing the average and inter-quartile range of yearly area estimations based on the backscatter values from SAR images from Sentinel-1, using Otsu thresholding.

### 5.2.3. TIME SERIES OF OTSU THRESHOLDS

In Figure 5.11 the dynamic NDWI thresholds are plotted for the period 2014-2019, calculated for the images covering the Katha polygon. The thresholds seem to follow a seasonal trend just like the area estimations and the discharge. During the monsoon the thresholds are lower compared to the winter months. The cause of this seasonality was not investigated. Nevertheless it could be argued that possible causes include a seasonal change in vegetation, humidity of the ground, atmospheric effects or otherwise.

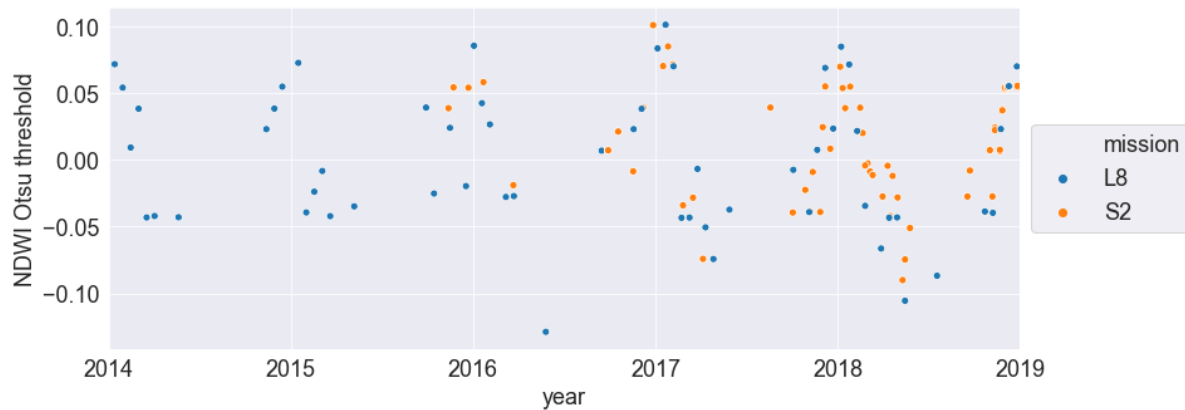


Figure 5.11: Time series of NDWI thresholds calculated with the Otsu method for the multispectral satellites Landsat 8 and Sentinel-2.

In Figure 5.12 the dynamic backscatter thresholds are plotted for the period 2014-2019, calculated for the images covering the Katha polygon. The same as for the NDWI threshold values in Figure 5.11 the thresholds seem to follow a seasonal trend. During the monsoon the threshold values are high compared to the winter months. The same as for the NDWI thresholds, these variations can be caused by vegetation or humidity of the ground, furthermore the incidence angle can have significant effects on SAR backscatter following [Panchagnula et al. \(2012\)](#). Waves on the water surface can also cause a higher backscatter, which are often induced by the wind.

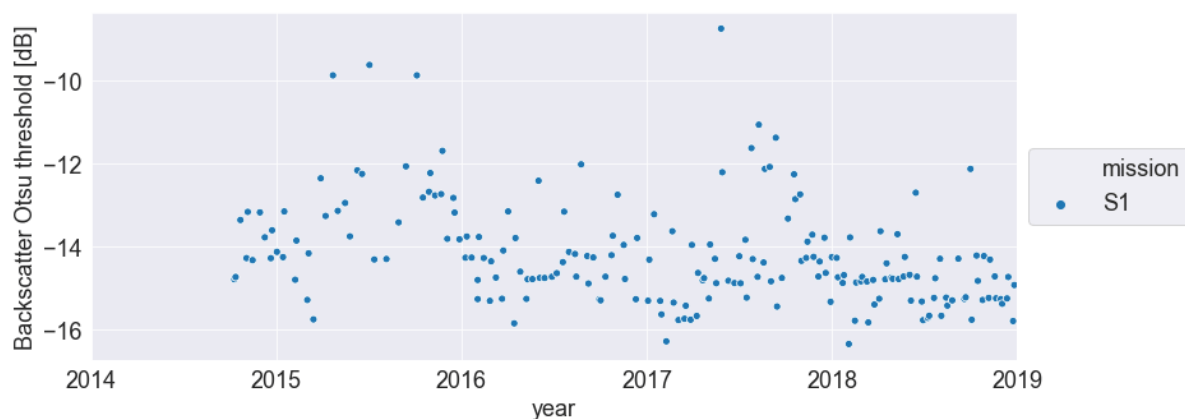


Figure 5.12: Time series of backscatter thresholds calculated with the Otsu method for the Sentinel-1 satellite.

As shown in figures 5.11 and 5.12, where a time series is plotted of the Otsu threshold values, the thresholds seem to follow a seasonal trend. In figures 5.13 and 5.14 the average and inter-quartile ranges of the threshold values are plotted for each month. The boxplot for the multispectral satellites shows a gap in the months June to August, but the seasonality is still visible. In the winter months the figure show higher threshold values compared to the months just before summer. For the microwave backscatter no seasonal trend is visible. The threshold varies irregular between -14 and -16 dB the whole year round.

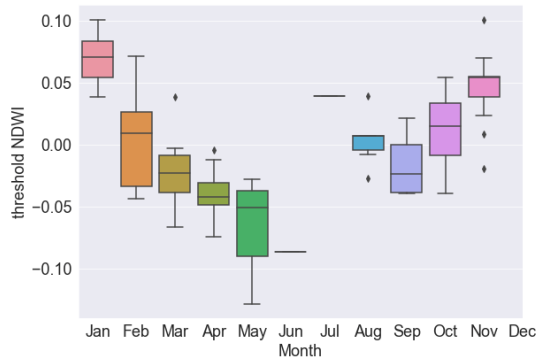


Figure 5.13: Boxplot of average NDWI Otsu threshold values from 2014-2019.

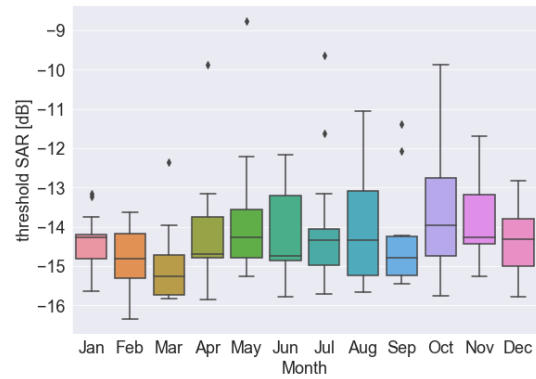


Figure 5.14: Boxplot of average backscatter Otsu threshold values from 2014-2019.

### 5.3. OUTLIER DETECTION AND TREND FITTING

In this section first the outliers that visually deviate from the other measurements were investigated case by case. Based on the causes of these deviation, some data points were removed and others were stated to be correct measurements. When all outliers have been removed a seasonal trend was fitted on the remaining data.

#### 5.3.1. EXAMPLES OF POSSIBLE OUTLIERS

A quick look at the time series from both the area estimations and the Otsu thresholds, showed that there were some data points that did not follow the (seasonal) trend. These area estimations or threshold values diverged from the other data points. To investigate whether the divergent points were indeed outliers and what could have caused the outlier, images that are assumed to be correct were compared to the possible outliers. This was done by looking at the RGB image, NDWI/backscatter image and the histogram taken from the edges of the river. The dates which were used are summarised in Table 5.2. These specific investigations show that the most occurring reason for the deviations are caused by flooding of the river.

Date	Satellite	Area [ $km^2$ ] with fixed th	Otsu threshold	Area [ $km^2$ ] with Otsu threshold
07-03-2018	S2	4.058	-0.022	4.035
19-08-2017	S2	12.102	0.039	11.577
17-02-2018	S1	5.541	-15.718	5.067
19-08-2017	S1	10.685	-14.760	10.732
30-04-2018	S1	4.364	-15.248	4.292
08-10-2017	S1	4.633	-11.747	7.248

Table 5.2: Some data points that are divergent from the other data points in the time series in figures 5.11 and 5.12.

#### 07-03-2018: A NORMAL DAY?

The time series in Figure 5.6 was used to choose a data point which was assumed to be a reliable measurement. The area estimation on 07-03-2018 is in line with the other measurements, which follow the seasonal trend, so this date is chosen as reference point for the other multispectral images that are discussed in this section. The false color composite and the NDWI image from 07-03-2018 are plotted in Figure 5.15 and 5.16. The histogram in Figure 5.17 shows a bimodal distribution of NDWI values, which makes it possible to use the single Otsu method to derive the threshold value to separate water from non-water pixels. The estimated threshold value is -0.022 as shown in Table 5.2.

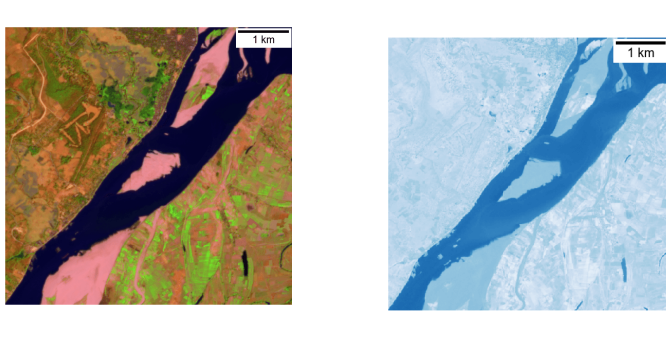


Figure 5.15: False color composite, made with the 'swir', 'nir' and 'green' bands of the Sentinel-2 image covering the Katha polygon on 07-03-2018.

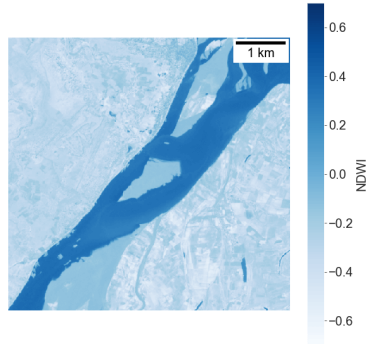


Figure 5.16: NDWI calculated from a Sentinel-2 image covering the Katha polygon on 07-03-2018.

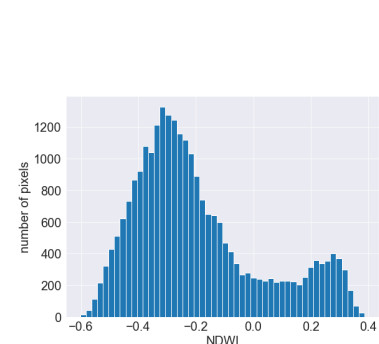


Figure 5.17: Histogram of NDWI values on the edges of the river taken from a Sentinel-2 image covering the Katha polygon on 07-03-2018.

19-08-2017: FLOODING

On 19-08-2017 a very high surface area of  $11.5 \text{ km}^2$  was estimated. The RGB image in Figure 5.18 shows that this high estimate was caused by the flooding of the river. The flooded area is even bigger than the Katha polygon. The histogram in Figure 5.20 shows a bimodal distribution of NDWI values and the threshold was estimated to be 0.039, which is indeed right in the middle of the valley of the histogram.

Because the flooded area extends the boundaries of the polygon, the total area of land covered with water was even higher than the area estimation shown in Table 5.2 and in the time series in sections 5.2.1 and 5.2.2. The high area estimation is not a measuring mistake, because the water is present. On the other hand it is up for discussion if the measurements of floods should be used, because the flooded area is not part of the river geometry, stated that the river is the area between the levees. Nevertheless the calculations taken during the floods will not be removed, because they are important to understand when floods have occurred. After a flood the river geometry is often changed, which influences the relation between discharge and river geometry.

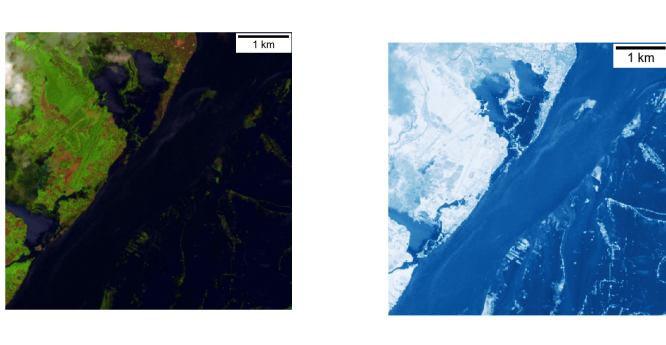


Figure 5.18: False color composite, made with the 'swir', 'nir' and 'green' bands of the Sentinel-2 image covering the Katha polygon on 19-08-2017.

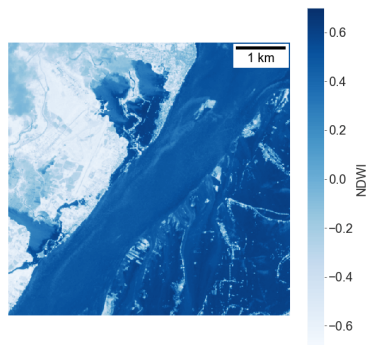


Figure 5.19: NDWI calculated from a Sentinel-2 image covering the Katha polygon on 19-08-2017.

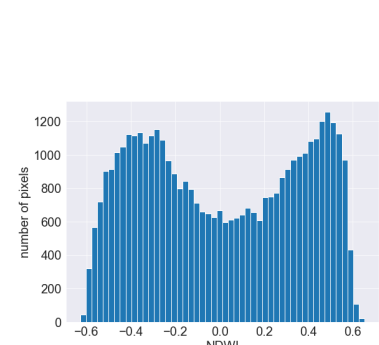


Figure 5.20: Histogram of NDWI values on the edges of the river taken from a Sentinel-2 image covering the Katha polygon on 19-08-2017.

### 17-02-2018: A NORMAL DAY?

For the multispectral images the Sentinel-2 image from 07-03-2018 was used as reference image for the multispectral images, and in the same way the image taken by Sentinel-1 on 17-02-2018 was chosen as reference to the other Sentinel-1 images. In the backscatter image from Figure 5.21 the river can be easily distinguished from the surrounding areas by the low backscatter values. The histogram in Figure 5.22 shows a bimodal distribution and with the single Otsu method the threshold is estimated to be -15.718 dB, as shown in Table 5.2.

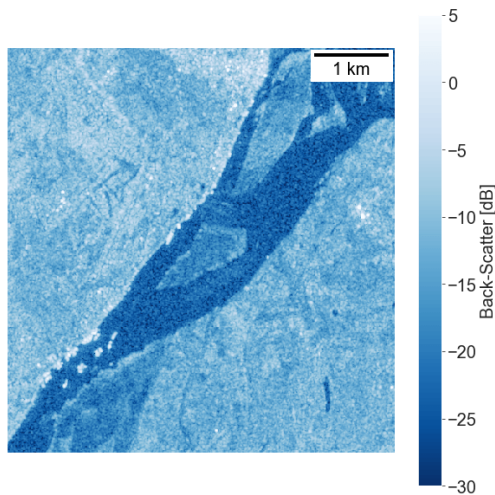


Figure 5.21: Backscatter plot of a Sentinel-1 image covering the Katha polygon on 17-02-2018.

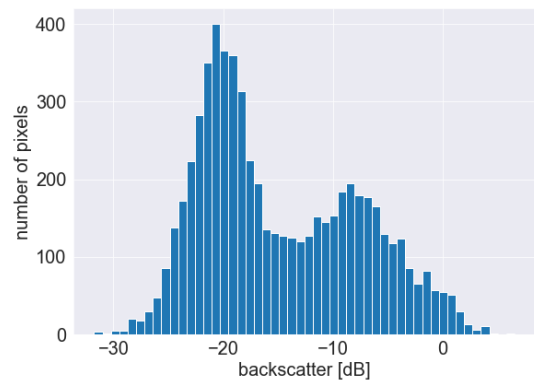


Figure 5.22: Histogram of backscatter values on the edges of the river taken from a Sentinel-1 image covering the Katha polygon on 17-02-2018.

### 19-08-2017: FLOODING

As shown in the backscatter image from 19-08-2017 in Figure 5.23 the river was flooded, resulting in a very high area estimation of  $10.685 \text{ km}^2$ , which is shown in the time series and in Table 5.2. The threshold estimated based on the histogram in Figure 5.24 is -14.760 dB. This flooded area was also shown in Figure 5.18 of the Sentinel-2 image taken on the same day.

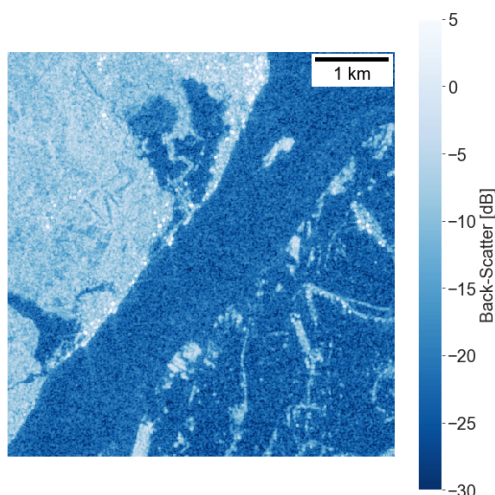


Figure 5.23: Backscatter plot of a Sentinel-1 image covering the Katha polygon on 19-08-2017.

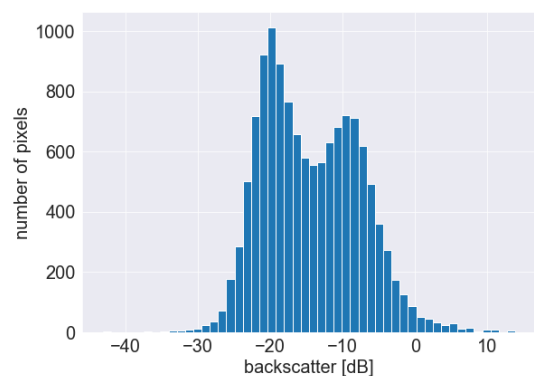


Figure 5.24: Histogram of backscatter values on the edges of the river taken from a Sentinel-1 image covering the Katha polygon on 19-08-2017.

### 08-10-2017: HIGH THRESHOLD VALUE

The threshold value estimated from the Sentinel-1 image taken on 08-10-2017 had a very high value of -11.747 dB compared to most Sentinel-1 images. As shown in the time series of the threshold values used for the Sentinel-1 images in Figure 5.12, roughly most threshold values are estimated between -14 and -16 dB. In the backscatter image in Figure 5.25 some light blue areas corresponding to backscatter values around -5 dB can be seen over the river, this made it harder for the Edge detector to detect the edges of the river. This resulted in a limited amount of pixels available for the histogram in Figure 5.26, causing a high threshold value. A possible cause of the areas with a higher backscatter value over the river can be waves in the water, caused by wind. Furthermore vegetation might have influenced this image.

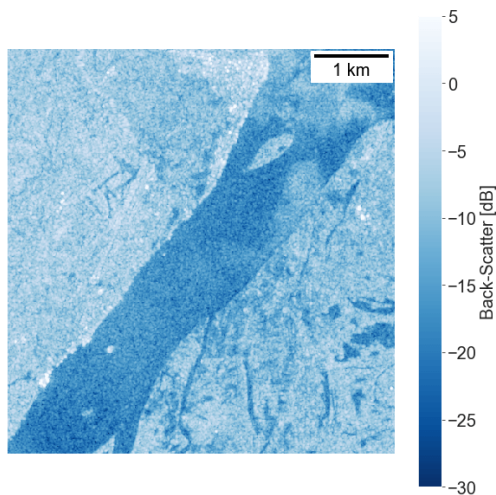


Figure 5.25: Backscatter plot of a Sentinel-1 image covering the Katha polygon on 08-10-2017.

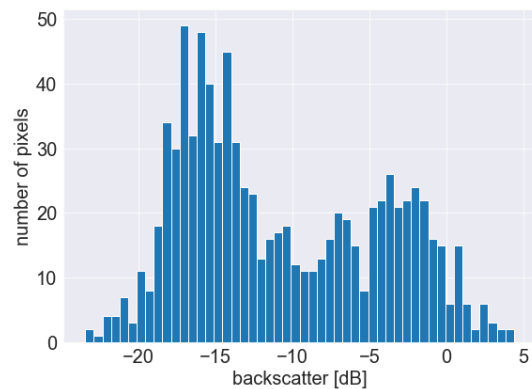


Figure 5.26: Histogram of backscatter values on the edges of the river taken from a Sentinel-1 image covering the Katha polygon on 08-10-2017.

### 5.3.2. SEASONAL TREND FIT

From the time series of the raw data in figures 5.6 and 5.1 a trend and seasonality can be derived. This trend and seasonality are shown in the boxplots from Section 5.2.1 and 5.2.2. The combination of trend and seasonality are plotted in the black line for the multispectral satellites and in grey for the Sentinel-1 satellites in figures 5.27 and 5.28. The figures show that using the Otsu threshold results in more overlap between the trends, than when using a fixed threshold. When optical images are combined with microwave images it is therefore better to use Otsu thresholding instead of fixed thresholding. Nevertheless the trends still deviate from each other. Especially in the months outside of the monsoon the estimations based on Sentinel-1 images show higher area estimations than the estimations based on multispectral images. This problem should be solved before they can be really combined together in estimating river area.

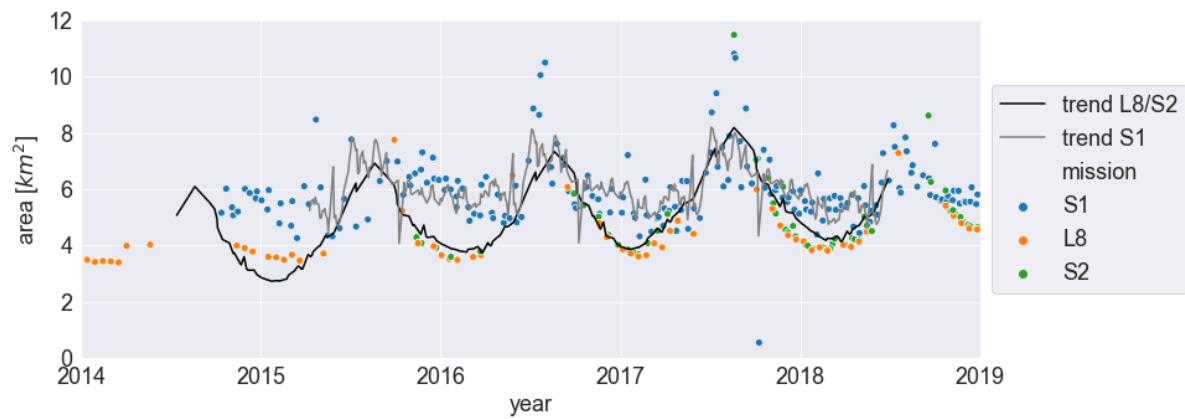


Figure 5.27: Time series of river area calculated with images from different satellite missions using Otsu thresholding at the Katha region from 2014-2019. The black line shows the 'trend + seasonality' of the multispectral images and the grey line shows the 'trend + seasonality' of the Sentinel-1 images.

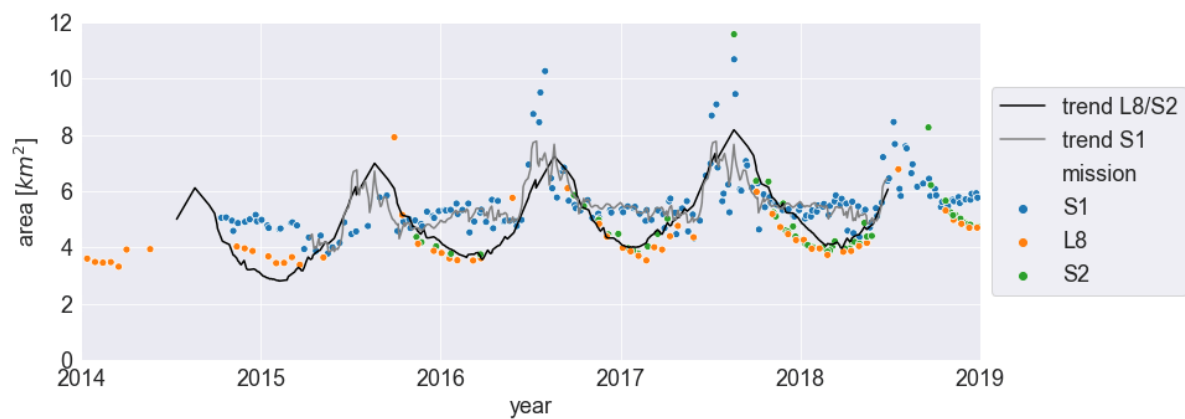


Figure 5.28: Time series of river area calculated with images from different satellite missions using a fixed threshold at the Katha region from 2014-2019. The black line shows the 'trend + seasonality' of the multispectral images and the grey line shows the 'trend + seasonality' of the Sentinel-1 images.

## 5.4. SENSITIVITY ANALYSIS ON THRESHOLDING

To investigate the influence of the threshold value on the river area estimations, a sensitivity analysis has been performed. First some cross-sections have been plotted to show how NDWI and backscatter values vary over the cross-section at Katha in both time and space. As a next step the Sentinel-2 image from 05-02-2017 was chosen as case study to investigate the effect of varying the NDWI/MNDWI threshold. For this day histograms were plotted of the NDWI and MNDWI values. Furthermore for different NDWI and MNDWI threshold values the edges along the river were plotted and the corresponding areas were calculated. This same procedure was performed for the Sentinel-1 images from 08-02-2017 to investigate the effect of varying the backscatter threshold value.

### 5.4.1. CROSS-SECTIONS

To see how the indexes vary over the river cross-section at Katha, the mean and standard deviation of NDWI values over the cross-section are plotted in Figure 5.29. These figures were made with all 'clear' images captured by either Landsat 8 or Sentinel-2 in the year 2017, and in total 27 images were used. The thick black line shows the average index value and the light blue area shows the standard deviation. On average the NDWI of the river is around 0.4 with a standard deviation of around 0.1. It should be taken into account that most images from Landsat 8 and Sentinel-2 were made outside the monsoon season, because most images during the monsoon were covered by clouds. Figure 5.29 therefore only gives information about the rest of the year.

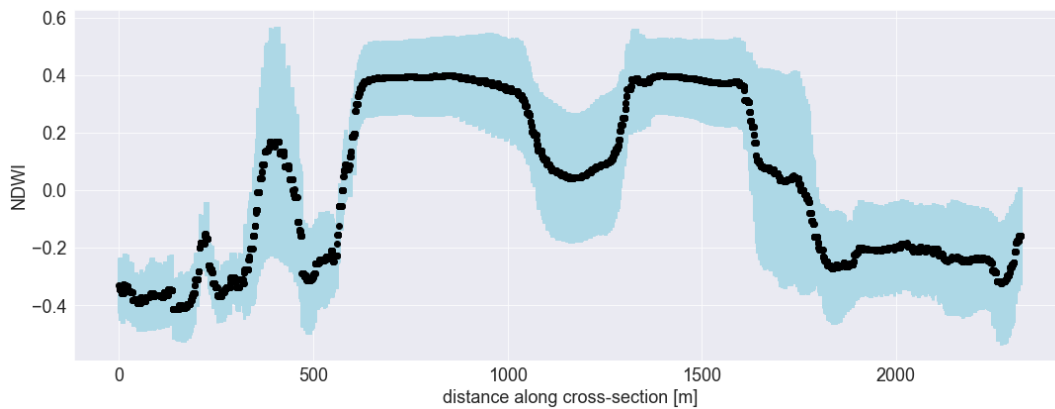


Figure 5.29: Average and standard deviation of NDWI values over the cross-section near Katha for the year 2017.

To get an idea on how the cross-sections differ in time, some different days from 2017 were selected and plotted in Figure 5.30. The figure shows the same pattern of a river with two main channels indicated by the high NDWI values for most of the days. Nevertheless the NDWI values differ between the days, which could be the result of atmospheric effects. Furthermore 19-08-2017 deviates from the other days, because the river was flooded, which is shown by the high NDWI value over almost the entire cross-section.

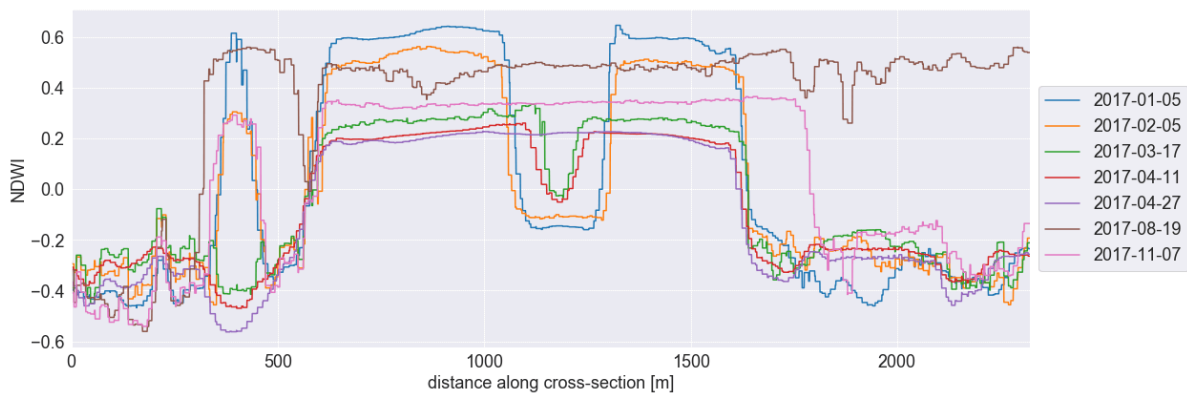


Figure 5.30: Cross-sections of NDWI values for 7 different days in 2017.

The downward peak in the middle of the Katha cross-section can be caused by the bank in the middle of the river as shown in Figure 5.32. This bank can be migrated from upstream or was covered with water during high discharge and dry when the discharge was low. The bank has a higher NDWI value than the land outside of the river.

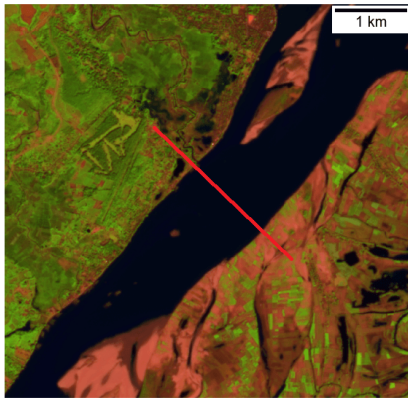


Figure 5.31: False color composite of Katha, made with the 'swir', 'nir' and 'green' bands of the Sentinel-2 satellite covering the Katha region when the river is wide and no bar is visible on 07-11-2017.



Figure 5.32: False color composite of Katha, made with the 'swir', 'nir' and 'green' bands of the Sentinel-2 satellite covering the Katha region when there is a bar in the middle of the river on 07-11-2017.

In the same way the NDWI and MNDWI were plotted over the cross-section near Katha, this method was also performed with images from Sentinel-1. In Figure 5.33 the back-scatter values over the cross-section near Katha are plotted. The average back-scatter is plotted in black and the standard deviation of the back-scatter is shown in light blue. The average backscatter of the river is -15 dB with a standard deviation of 10 dB. The measurements were all from the year 2017 when 82 Sentinel-1 images were available. The figure shows the same pattern as the cross-section plots of the NDWI values. The only difference is that the bar in the middle of the river is less distinctive in the Sentinel-1 cross-sections. The bank can be a very water saturated surface, which causes a low backscatter close to the backscatter of water.

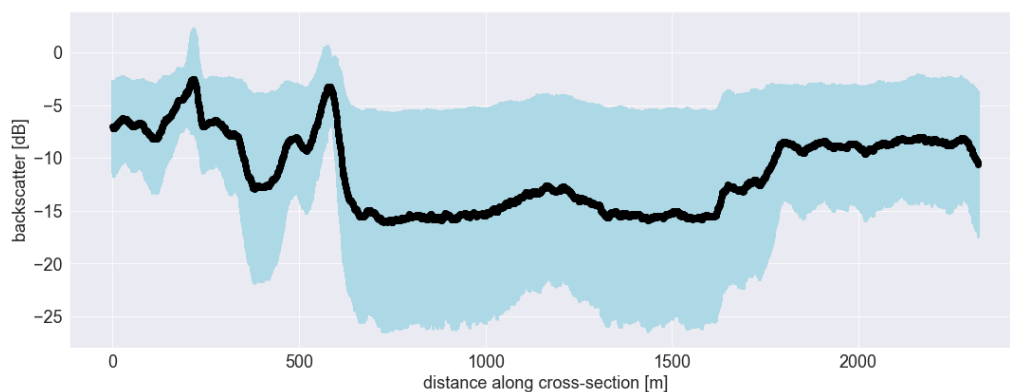


Figure 5.33: Average and standard deviation of backscatter values over the cross-section near Katha for the year 2017.

In both the NDWI and the backscatter plots, the cross-sections show a steep gradient at the boundaries between water and land. In figures 5.34 and 5.35 close-ups are shown of the Katha cross-section from 500 to 700 meters. The NDWI changes from -0.2 to 0.4 in the region from 550-620 meter. This gradient shows that if the threshold estimation is slightly off, this has a big influence on where the location of the river edge is estimated. For the backscatter the steep gradient is from 570-650 meter. At this location the backscatter decreases from -5 dB to -15 dB. Most interestingly the NDWI shows a constant gradient in NDWI values, whereas the backscatter shows a peak at this location. Because for both the NDWI and backscatter different days were used to calculate the mean and standard deviation and the backscatter includes more days and more monsoon days, these images can not be compared to each other. For a better comparison only the days that both Landsat 8/Sentinel-2 and Sentinel-1 passed should be used, or only the images taken outside of the monsoon.

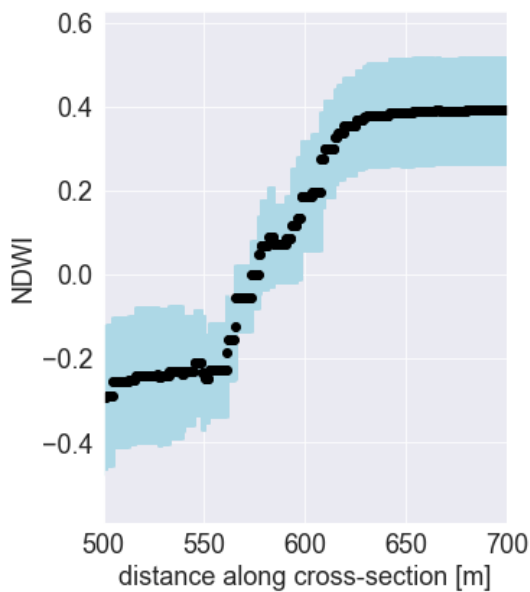


Figure 5.34: Close-up of the Katha cross-section from Figure 5.29 between 500 and 700m showing the average and standard deviation of NDWI values for all clear images in 2017.

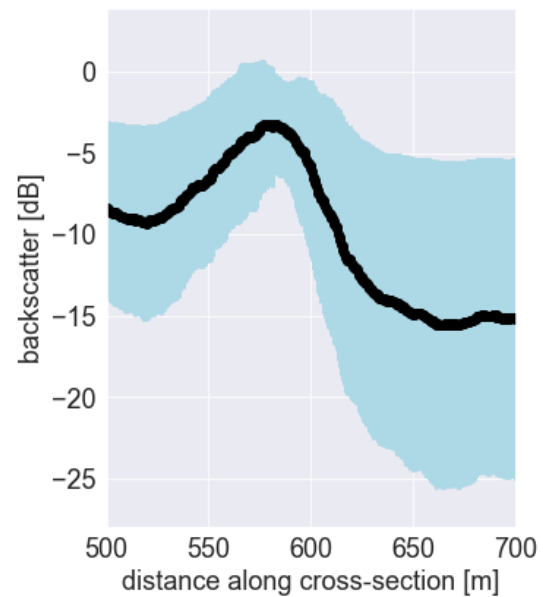


Figure 5.35: Close-up of the Katha cross-section from Figure 5.33 between 500 and 700m showing the average and standard deviation of backscatter values for all Sentinel-1 images from 2017.

#### 5.4.2. CASE STUDY ON NDWI THRESHOLD SENSITIVITY: KATHA 05-02-2017

For this case study a multispectral image covering the Katha polygon from 05-02-2017 was used. In the figures below the NDWI (Figure 5.36), MNDWI (Figure 5.37) and a false color composite using the 'swir', 'nir' and 'green' band (Figure 5.38) are given to get a feeling of how this day looked like. The false color composite shows that this day was very clear, because no clouds are visible.

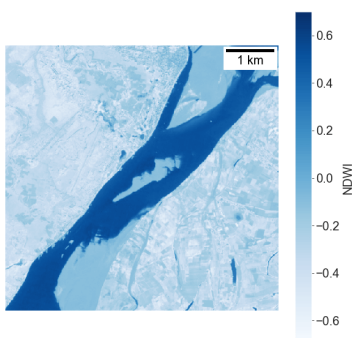


Figure 5.36: NDWI values in the Katha polygon calculated from Sentinel-2 image from 05-02-2017.

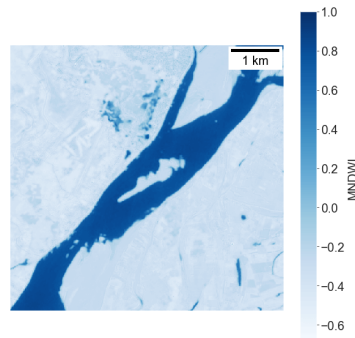


Figure 5.37: MNDWI values in the Katha polygon calculated from Sentinel-2 image from 05-02-2017.



Figure 5.38: False color composite using the 'swir', 'nir' and 'green' band in the Katha polygon calculated from Sentinel-2 image from 05-02-2017.

## HISTOGRAMS

In figure 5.39 and 5.40 histograms are plotted of the NDWI and MNDWI values from Figure 5.36 and 5.37. In general the two peaks in both histograms represent the 'non-water' pixels on the left and the 'water' pixels on the right. To separate these two classes the estimated Otsu threshold will be in between the two peaks of the histograms. Nevertheless the histograms show a wide bandwidth of values that could be used to separate the two peaks from each other. Furthermore, the NDWI histogram shows an extra small peak around -0.1 NDWI, which could impact the single Otsu calculation. These histograms represent all pixels from the images.

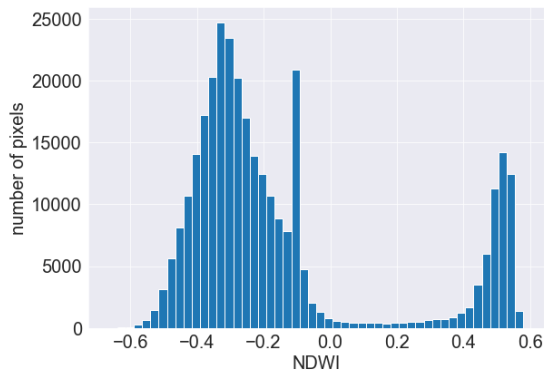


Figure 5.39: Histogram of NDWI values in the Katha geometry on 2017-02-05.

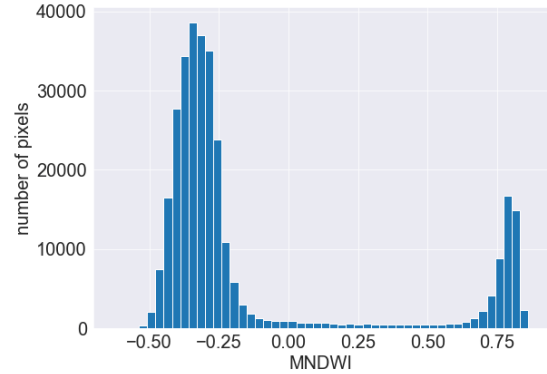


Figure 5.40: Histogram of MNDWI values in the Katha geometry on 2017-02-05.

To calculate the Otsu threshold, first the Canny edge detector was applied and the pixels on the edges result in the histogram of NDWI values in Figure 5.41 and MNDWI values in Figure 5.42. In those figures the peaks are much closer together than in figures 5.39 and 5.40 and the Otsu threshold can be calculated. The resulting threshold values are given in Table 5.3. The MNDWI has a higher threshold value, than the estimated NDWI threshold value. These values correspond to the estimation from Huang *et al.* (2018) that for the NDWI a threshold of 0 is usually good and for MNDWI this is 0.2.

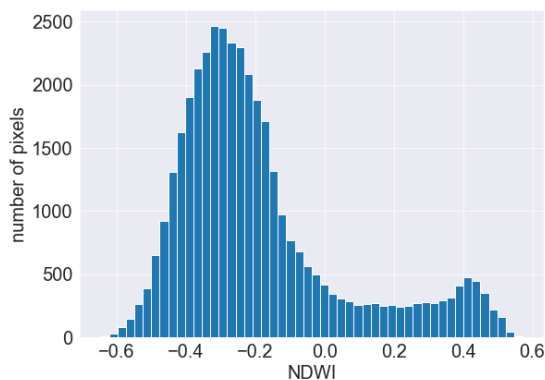


Figure 5.41: Histogram of NDWI values on the edges of the river taken from a Sentinel-2 image covering the Katha polygon on 2017-02-05.

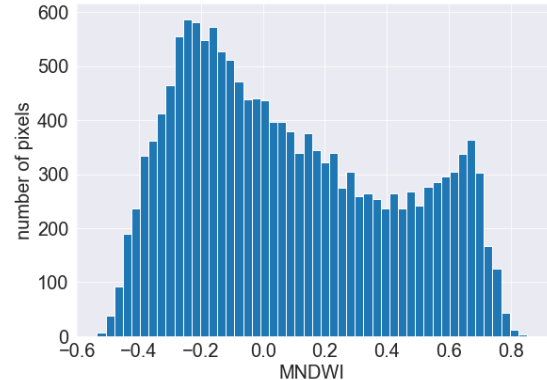


Figure 5.42: Histogram of MNDWI values on the edges of the river taken from a Sentinel-2 image covering the Katha polygon on 2017-02-05.

Method	Threshold
NDWI	0.085
MNDI	0.228

Table 5.3: Otsu threshold values for NDWI and MNDWI over the region around Katha calculated with the Canny Edge detector and the single Otsu method.

### EDGE DETECTION

To investigate the influence of the threshold value on the estimation of river area, for both the NDWI and MNDWI a close-up of the water edges is plotted for some different threshold values, as shown in figures 5.43 and 5.44. Furthermore the NDWI and MNDWI edges from the threshold as calculated in Table 5.3 are compared in Figure 5.45 with a false color composite from the 'nir', 'swir' and 'green' band as background. Figures 5.43 and 5.44 show that the higher the threshold, the more the edge moves inside to the river. In Figure 5.45 it is shown that using the calculated Otsu thresholds from Table 5.3, both the NDWI edge and MNDWI edge are roughly on the same location, but do follow a different pattern. The MNDWI edge is much smoother than the NDWI edge. This difference can be caused by the fact that the 'swir' band, used in the MNDWI, is less sensitive to optical active constituents than the 'nir' band that is used in the NDWI. Looking at Figure 5.45 the Irrawaddy river might have a lot of optical active constituents around the edges of the river. In this case the NDWI shows a more accurate result than the MNDWI, when comparing the edges to the background of the image. When comparing the edges for different NDWI and MNDWI threshold values, the edge shifts between 2-5 meters when the threshold varies with 0.1 for both the NDWI and the MNDWI.

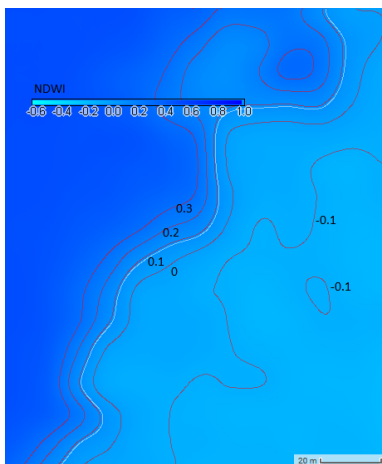


Figure 5.43: Edges of the water based on different NDWI threshold values. From left to right the red lines represent the threshold values of 0.3, 0.2, 0.1, 0 and -0.1 and in white the Otsu threshold of 0.085 is plotted with NDWI in the background.

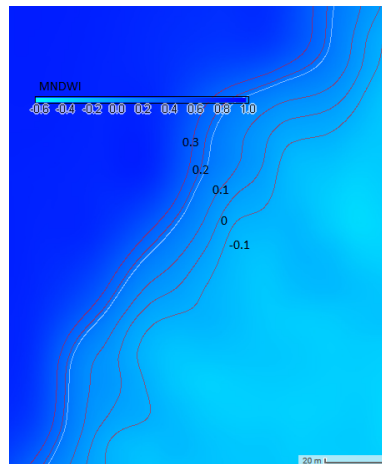


Figure 5.44: Edges of the water based on different MNDWI threshold values. From left to right the red lines represent the threshold values of 0.3, 0.2, 0.1, 0 and -0.1 and in white the Otsu threshold of 0.228 is plotted with MNDWI in the background.



Figure 5.45: In grey the MNDWI edge when using the Otsu threshold of 0.228 and in red the same for the NDWI using a threshold of 0.085. The background is a false color composite using 'nir', 'swir' and 'green' bands.

### AREA CALCULATION

For different threshold values of NDWI and MNDWI the edges of the water were plotted in figures 5.43 and 5.44. The area of the river within the Katha polygon is plotted in Figure 5.46 for different NDWI and MNDWI threshold values. The figure shows that for both indexes the estimated area of the river decreases when a higher threshold value is used. It is interesting to see that between 0 and 0.3 the lines of the NDWI and MNDWI show the same trend.

In Figure 5.47 a close-up of Figure 5.46 is plotted for the threshold values between 0 and 0.35 and a linear trend line is added. This figure shows that the two lines are not exactly the same. The estimated area based on MNDWI is bigger than the estimation area based on NDWI for the same threshold value. This trend line shows that when the threshold value for the MNDWI is changed with 0.1 the area decreases with  $0.012 \text{ km}^2$ . When the NDWI threshold is 0, a threshold of 0.05 would give the same area estimation using the MNDWI. This value is much lower than the 0.2 threshold for MNDWI stated in Huang *et al.* (2018).

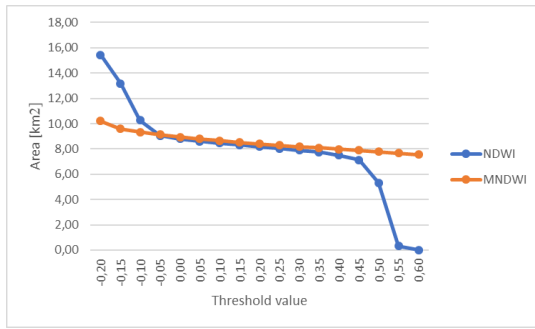


Figure 5.46: Area estimations of the Irrawaddy river in the Katha polygon for different threshold values on 2017-02-05 for both NDWI and MNDWI.

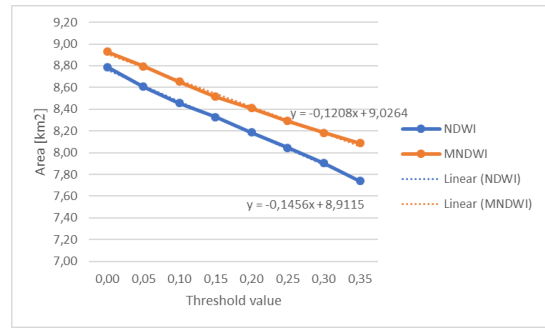


Figure 5.47: Area estimations of the Irrawaddy river in the Katha polygon for different threshold values on 2017-02-05 for both NDWI and MNDWI in the range from 0 to 0.35 to investigate the linearity.

### 5.4.3. CASE STUDY ON BACKSCATTER THRESHOLD SENSITIVITY: KATHA 08-02-2017

The same as for the case study on the sensitivity of the NDWI and MNDWI threshold value, a case study on the sensitivity of the backscatter threshold on river area estimation has been performed using a Sentinel-1 image from 08-02-2017.

#### BACKSCATTER IMAGE AND HISTOGRAM

In figure 5.48 the backscatter values from the Sentinel-1 image from 08-02-2017 and in figure 5.49 the histogram of backscatter values corresponding to this image are plotted. In the backscatter image the river is clearly visible because of its low backscatter values. The surrounding land has higher backscatter values than the water. In the histogram the non-water pixels are represented by the right big peak around -10 dB and the left peak represents the river. Using the Otsu method, the backscatter threshold of this image is -16.255 dB.

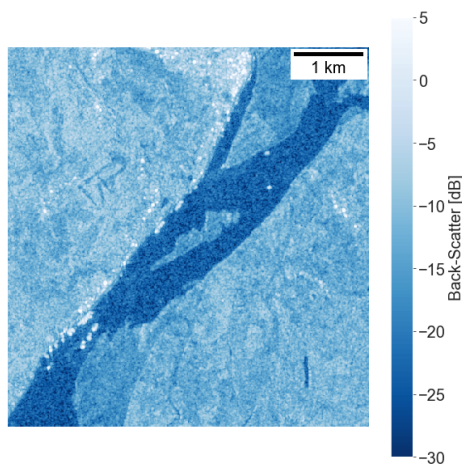


Figure 5.48: Backscatter plot of a Sentinel-1 image covering the Katha polygon on 08-02-2017.

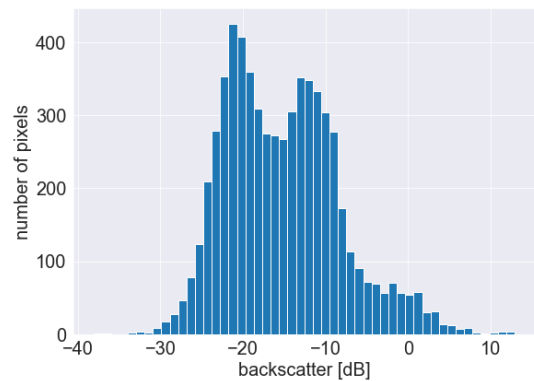


Figure 5.49: Histogram of backscatter values on the edges of the river taken from a Sentinel-1 image covering the Katha polygon on 08-02-2017.

#### EDGE DETECTION AND AREA CALCULATION

In Figure 5.50 the edges of the water when using different backscatter threshold values are plotted to show how much the edge location changes when using a different threshold value. The red lines represent threshold values ranging from -18 to -14 dB and the white line is the edge when using the threshold value of -16.255 dB, calculated using Canny Edge detection and Otsu thresholding on the image from Figure 5.48. The distances between the edges are between 2-5 meters, depending on the location. This means that when the threshold values is around 1dB off, this can result in more than a meter difference in river width estimation.

In Figure 5.51 for different backscatter threshold values, the corresponding river area within the Katha polygon is plotted. The plot shows that when the threshold value increases, the estimated area increases following a polynomial function. In Figure 5.50 it was also shown that when the threshold increases, the edge moves outward of the river, resulting in a higher area estimation. Because water has a very low backscatter, using a to high backscatter threshold value can resulting in misclassifying land as water.

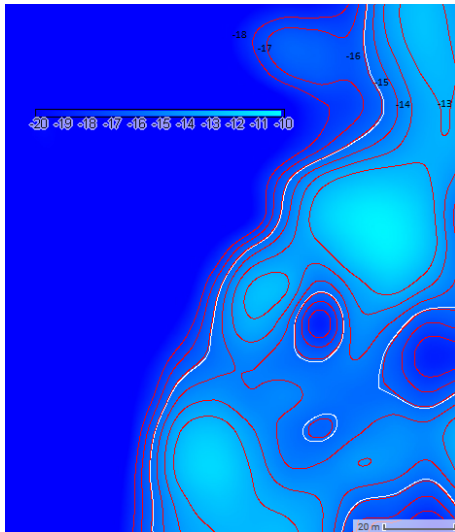


Figure 5.50: Edges of the water based on different backscatter threshold values. From left to right the red lines represent the threshold values of -14 to -18 dB white the Otsu threshold of -16.255 dB is plotted with backscatter values in the background.

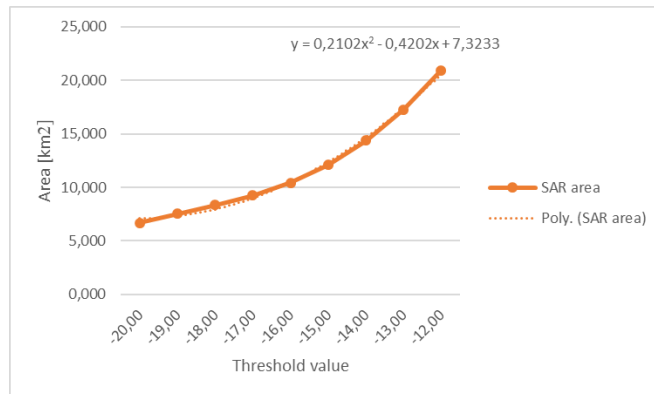


Figure 5.51: Area estimations of the Irrawaddy river in the Katha polygon for different backscatter threshold values on 2017-02-08.

#### VARIABLES THAT CAN INFLUENCE THE BACKSCATTER THRESHOLD

All Sentinel-1 images that were used for this thesis had instrumentmode 'VV' and swathmode 'IW', so the influence of different instrumentmode or swathmode was not investigated. Nevertheless other variables did change between acquisitions. The variables that change were the orbit properties (ascending or descending) and the sun angle. These two might influence the calculated Otsu threshold and therefore the estimated area. In Figure 5.52 the backscatter threshold is plotted against the estimated area. This figure shows no clear correlation between those properties. Also there is no difference between the measurements taken during ascending and descending orbit. In Figure 5.53 the Otsu threshold is plotted against the sun angle. The smaller the angle of the sun, the lower the Otsu threshold. This is indeed the seasonal variation which was shown before in Figure 5.14. In Figure 5.54 the sun angle is plotted against the estimated area. This figure is also a result of the seasonal variation as shown in Figure 5.8. The most interesting feature of this figure is that the area estimation based on a fixed threshold show less spread in measurements than the area estimations based on Otsu thresholding.

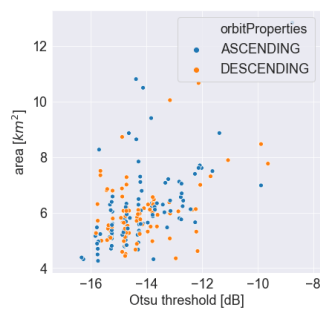


Figure 5.52: Backscatter Otsu threshold vs estimated river area.

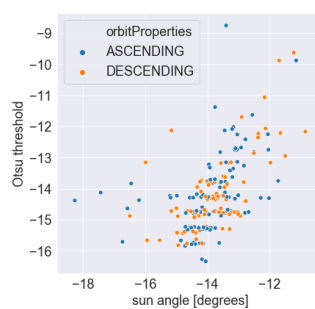


Figure 5.53: Backscatter Otsu threshold vs sun Angle.

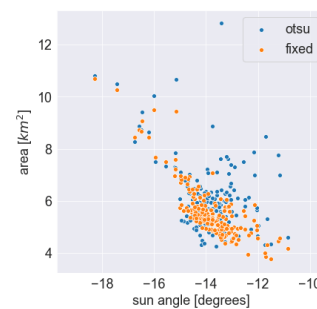


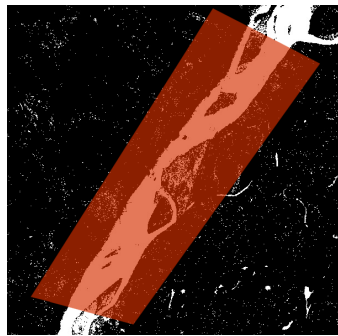
Figure 5.54: Sun angle vs estimated river area.

#### 5.4.4. MASK COMPARISON

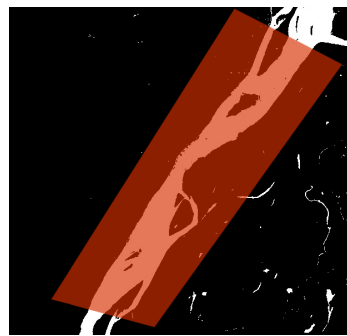
Figure 5.61 shows that the areas estimated from Sentinel-1 images are often larger than the areas estimated with one of the multispectral satellites. Figure 5.55 shows the water pixels in white for 16-04-2018 calculated from both Sentinel-1 and Sentinel-2 images of the Katha region. In Table 5.4 the Otsu thresholds and the estimated area are given for every figure.

	Otsu threshold	area [ $km^2$ ]
(a) SAR	-16.743	10.646
(b) NDWI	-0.0495	9.834
(c) MNDWI	0.0401	9.477

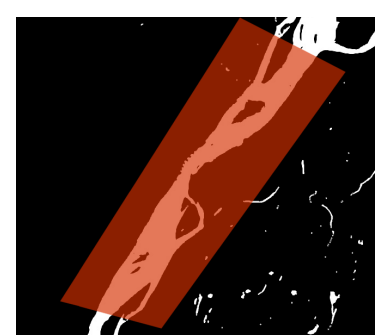
Table 5.4: Threshold values and estimated areas for the figures in Figure 5.55.



(a) Water pixels based on backscatter values from Sentinel-1 image.



(b) Water pixels based on NDWI values from Sentinel-2 image.



(c) Water pixels based on MNDWI values from Sentinel-2 image.

Figure 5.55: Water pixels (white) based on Otsu thresholds from Table 5.4 for images taken on 16-04-2018 with Sentinel-1 and Sentinel-2.

In Figure 5.56 a close-up of the Katha region is shown with the edges of the NDWI, MNDWI and backscatter values based on the threshold values in Table 5.4. The backscatter edges are clearly more noisy and also covers areas outside of the river, causing the higher estimations in river area.

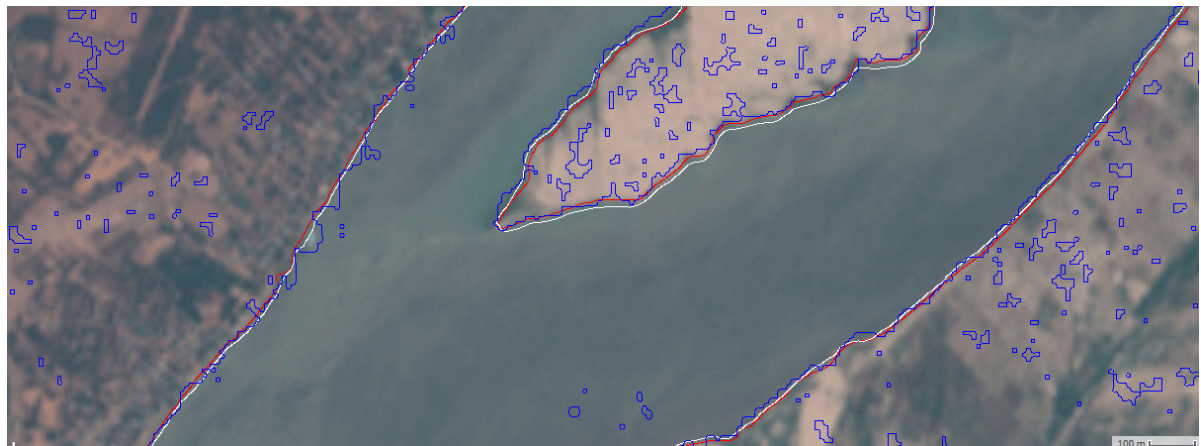


Figure 5.56: Close-up of RGB image in the region of Katha with the edges calculated with the threshold values in table 5.4 for the NDWI (red), MNDWI (white) and backscatter (blue).

## 5.5. RIVER AREA VS DISCHARGE

In Figure 5.57 a time series is shown of the discharge and river area estimations based on multispectral images at Katha for the period 1996-2010, which is the period that GRDC discharge data is available. During this period only the multispectral satellites Landsat 5 and Landsat 7 were available. It was not possible to use Sentinel-1 or more Landsat 8 images because the GRDC database is available until 2011 whereas the Sentinel-1 images are available from 2014 and Landsat 8 from 2013. The figure shows that in general a high discharge correlates to a larger river area. In this figure it is also visible that during the months with high discharge, fewer multispectral images were available. Furthermore the Landsat 7 estimations in Figure 5.57 are lower than the Landsat 5 estimations and this is caused by the SLC failure.

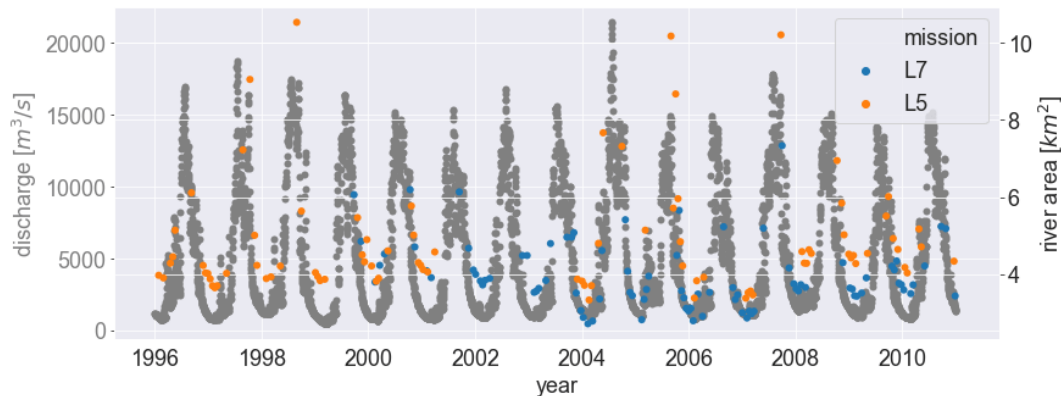


Figure 5.57: Time series of river discharge data from the GRDC database at Katha station, plotted together with river area estimations from the Katha polygon.

In Figure 5.58 the river area is plotted versus the discharge. This figure shows that in general a higher discharge results in a larger river area estimations. The straight line is the regression line with a 95% confidence interval. In Figure 5.57 some years have a higher area estimation during low discharge than other years. This can be caused by a change in river morphology. The river morphology is constantly changing, but after the floods in the monsoon, these morphological changes are largest. The changes in morphology influence the relation between river discharge and river area, which also results in the large spread in data in Figure 5.58.

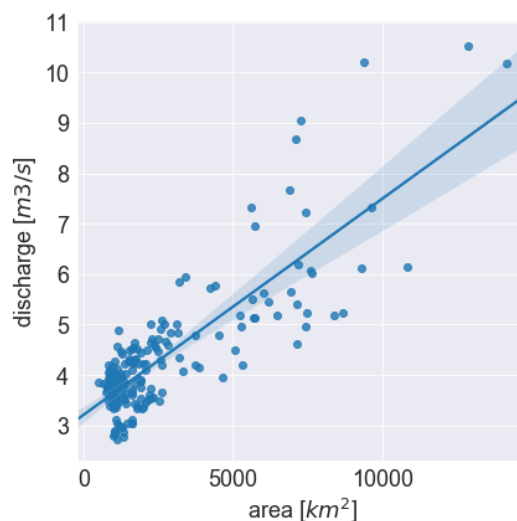


Figure 5.58: Joint distribution function showing the river area estimations, based on Landsat 7 and Landsat 5 multispectral images against the GRDC discharge data measured on the same days. The correlation between discharge and river area is 0.82.

## 5.6. CORRELATIONS

For different combinations of variables, joint distribution functions are plotted in this section. For every joint distribution the correlation coefficient ( $\rho$ ) was calculated. The red '1:1' lines represent the data if there is full correlation between the variables which is equal to 1.

### 5.6.1. FIXED THRESHOLD VS DYNAMIC THRESHOLD

In Figure 5.59 the river area estimations based on a fixed threshold of 0 for the multispectral images and -15 dB for the Sentinel-1 images, are compared to the the area estimations based on dynamic Otsu thresholding on the same images. The figure shows all area estimations from the period 2014-2019. In general the area estimations based on a fixed threshold correlate very well to the area estimations based on Otsu thresholding. Nevertheless there is a spread in the data, which is larger for the Sentinel-1 images ( $\rho = 0.71$ ) than for the multispectral images ( $\rho = 0.98$ ) This indicates that dynamic thresholding more important when using microwave images, than when using multispectral images to calculate river areas.

### 5.6.2. NDWI vs MNDWI

To compare if using NDWI or MNDWI index gives similar result, the area estimations calculated with NDWI is scattered against the estimated areas based on MNDWI in Figure 5.60. This figure shows that using the NDWI gives very similar results to using the MNDWI, which is also shown by the correlation coefficient of 0.98. For this region both NDWI and MNDWI could be used to estimate river areas.

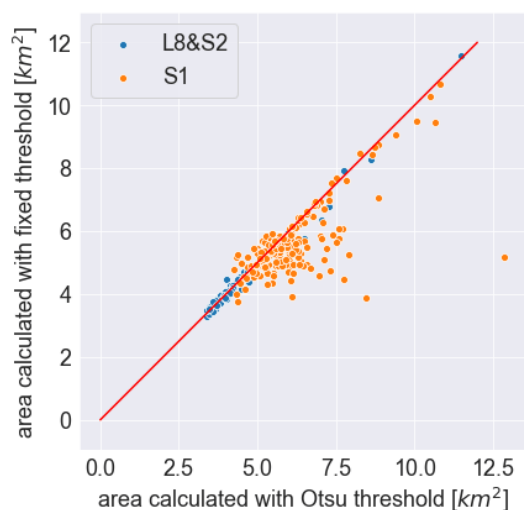


Figure 5.59: River area estimations in the Katha polygon. The orange dots represent the estimations based on microwave images from Sentinel-1 and the blue dots show the results based on optical images from Landsat 8 and Sentinel-2. The graph shows the influence of using a fixed threshold or dynamic threshold. The L8/S2 result have a correlation of 0.98 and the S1 result a correlation of 0.71 between the area calculations based on a fixed or Otsu threshold.

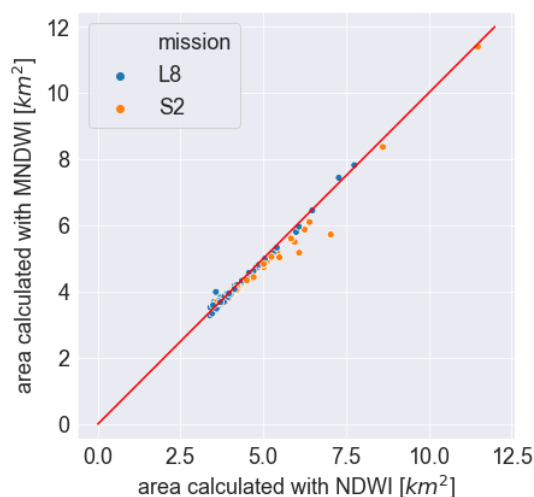


Figure 5.60: River area estimations in the Katha polygon. The orange dots represent the estimations based on Sentinel-2 images and the blue dots show the results based Landsat 8 images. The graph shows the influence of using NDWI or MNDWI for detecting water. The correlation between area calculated with NDWI and MNDWI is 0.98.

### 5.6.3. SENTINEL-1 VS SENTINEL-2&LANDSAT 8

In Figure 5.61 a scatterplot is shown which correlates the estimated areas based on multispectral images from Landsat 8 and Sentinel-2 with the estimated areas based on microwave images from Sentinel-1. For every day that both a Sentinel-1 image and a Sentinel-2 or Landsat 8 image was available the results are plotted in the graph. Unfortunately this does not happen very often, so only 27 days can be used from the period 2014-2019. The figure shows that for a dynamic threshold the estimated area based on Sentinel-1 images is often higher than the estimated area based on multispectral images from Landsat 8 and Sentinel-2. The red line shows the "1:1" line. The points should be on this line when there is a good correlation. The correlation between the area estimations based on SAR images and the MS images is higher when using a fixed threshold ( $\rho = 0.90$ ) than when using a dynamic threshold ( $\rho = 0.83$ ). This is in contradiction to the timeseries shown in Figure 5.28 and Figure 5.27 where the timeseries show more overlap, say a higher correlation, when Otsu thresholding is used. This difference can be caused by the fact that only 27 days were used, which does not give a good representation of the data. There are no data points during the monsoon, because no optical images are available during that period.

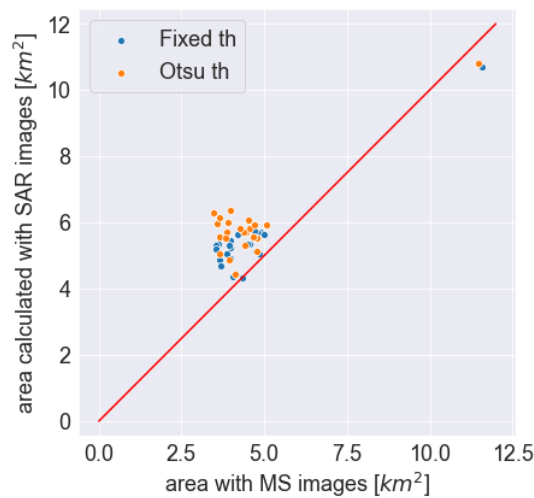


Figure 5.61: Joint distribution function between estimated areas based on multispectral images from Landsat 8 and Sentinel-2, and microwave images from Sentinel-1. The correlation between area estimations based on MS images and SAR images is 0.90 when using a fixed threshold and 0.83 when using Otsu thresholding.



# 6

## DISCUSSION

The approach of combining multispectral satellite images with microwave images to estimate river area on a regular basis shows reasonably accurate results, a critical evaluation of the study is performed in this chapter. On one hand, the chapter contains a reflection on the thesis, and on the other hand it is shown how the results contribute knowledge to the research area.

### AVAILABLE DATA AND VALIDATION

First of all, Landsat 8 and Sentinel-2 are not the only satellites that provide multispectral images. For example, other satellites are operational which also provide multispectral images for free such as MODIS and ASTER. Nevertheless those satellites have other spatial and temporal resolutions than Landsat, so extra investigation would be needed to add them to the method. Also Sentinel-1 is not the only satellite that provides microwave images. The addition of these other multispectral or microwave images could possibly improve the method, resulting in a higher spatial-temporal resolution.

Furthermore, no validation data was available to check if the river area estimations are correct. The only way to validate the area estimations was by comparing the estimations based on Sentinel-1 images to the area estimations based on multispectral images. This showed that the area estimations based on Sentinel-1 images are often much larger than the area estimations based on multispectral images, see Figure 5.61. Furthermore the relation between the river area and the river discharge was investigated using Landsat 7 and Landsat 5 images in Section 5.5. In the time period 1996-2011, when GRDC discharge data was available at Katha, the Landsat 8, Sentinel-1 and Sentinel-2 satellites were not operational yet. The SLC failure of Landsat 7 could have resulted in too low area estimations, making it harder to find a relation between river discharge and river area. Furthermore the uncertainty in the GRDC discharge data was not taken into account when investigating the relationship between river discharge and river area.

### CHOICE OF INDICES AND IMAGE SELECTION

For the multispectral images, only the NDWI and MNDWI indices were used to detect water. In literature many other indices have been investigated in the past years. For example in Fisher *et al.* (2016) seven water index methods were tested and the conclusion was that the accuracy of those indices was dependent on the composition of the validation pixels and there was no index performing best. For the method described in this thesis, also other indices could have been used.

For the Sentinel-1 images only the images with a 'VV' polarisation and 'IW' swathmode were selected. Following Vachon and Wolfe (2011) 'HH' polarization usually performs better in separating land from water under calm water conditions. The scattering of open water shows less scattering with the 'HH' polarization compared to the 'HV' or 'VV' polarization and is less sensitive to capillary waves created from wind. Unfortunately only images taken with 'VV' or 'VH' polarization were available for the Katha region. At other locations it might be useful to investigate the effects of using other polarisations.

### FLOODING AND OUTLIER DETECTION

When the river was flooded, the flooded area extended the Katha polygon, which was used to calculate the river area in this region. The area estimations during floods did not only contain the water inside the river, but also the water covering the floodplains. In the results, seasonal trends were shown which included the measurements during floods. For more accurate results a solution should be found on how to deal with the floods. The floods can not be treated as outliers because they are very important for the understanding of the hydrodynamics and morphodynamics of the river. Nevertheless they do have a big influence on the seasonal trend calculations.

Because most data points that deviated a lot from the seasonal trend were caused by flood events, which are no outliers, no further outlier detection has been performed. The data points, that were not floods, followed the seasonal trend quite well. Still it might have been useful to perform some outlier detection. This outlier detection can be based on how well the histogram shows a bimodal distribution. When the histogram is not bimodal, the estimated threshold value can be too high or too low, resulting in a wrong area estimation.

### HYDRODYNAMIC MODELLING

The main object of this thesis was to increase the spatial-temporal data availability of satellite images to improve hydrodynamic modelling. Section 5.5 showed that the relation between the river area and the discharge can change between consecutive years. This change might be caused by morphodynamic changes in the river, which occur mostly after the flood events in the monsoon. Following [Karpadne \*et al.\* \(2016\)](#) spatial-temporal monitoring of water body dynamics is very essential for understanding the global or regional water availability, which provides insight in the natural processes that shape the storage of water resources. In the Katha region the improvement of spatial-temporal monitoring is therefore very important, whereas in other regions in the world where the water body dynamics are more constant, this is less important.

### NOISE IN SENTINEL-1 IMAGES

The water mask in Figure 5.56 shows that the water mask from Sentinel-1 contains a lot of noise outside of the river. This noise is often classified as water, resulting in a too high area estimation which can also be seen in the time series in Figure 5.27 where the area estimations from Sentinel-1 are structurally higher than the estimations made with Sentinel-2 and Landsat 8 images. In order to be able to combine the multispectral images with the Sentinel-1 images a solution should be found on removing the noise in the water mask from the Sentinel-1 images. Another reason why Sentinel-1 images give higher area estimations is because optical images can not detect water underneath vegetation following [Guerschman \*et al.\* \(2011\)](#). If vegetation would cover the water, the water can still be detected by the SAR satellite because the microwave signal penetrates through vegetation. The optical sensor would classify this location as vegetation.

# 7

## CONCLUSIONS AND RECOMMENDATIONS

In this thesis, a method of combining satellite based optical and microwave remote sensing to estimate river geometry, has been explored. This chapter consists of two sections. Firstly, the research questions are answered. Thereafter recommendations for use and recommendations for future research are given.

### 7.1. CONCLUSIONS

The main question of this thesis was: *"How can satellite based optical and microwave images be combined to get a realistic estimation of river geometry to improve hydrodynamic modelling?"*. The main conclusion to this question is that river area estimations based on the multispectral satellites Landsat 8 and Sentinel-2, give slightly different results from the river area estimations, based on Sentinel-1 images. Both methods show the same seasonal trend, only the area estimations based on Sentinel-1 images outside the monsoon season are always higher than the area estimations based on multispectral images. As mentioned in the discussion, this bias can be caused by the noise in the Sentinel-1 images and more research is needed to solve this problem. Nevertheless this thesis did show that the results improve when dynamic Otsu thresholding is applied instead of using a fixed threshold for both the backscatter values and the NDWI values.

#### WHICH AVAILABLE SATELLITE DATA CAN BE USED TO GET GEOMETRIC INFORMATION OF A RIVER?

There are two sensors types which were used in this thesis for detecting surface water, namely optical and microwave sensors. The optical sensor is on board of the Landsat 8 and Sentinel-2 satellites and the microwave sensor is on board of the Sentinel-1 satellite. There are other satellites operational that also carry these kind of sensors, but they were not used for this thesis. The optical images can be used to calculate one of the different water indices, in this thesis the normalized difference water index (NDWI) was used. Water behaves different than (dry) land in the 'nir' and 'green' bands, which are used for calculating the NDWI. Furthermore water can be detected by the very low backscatter values measured with the microwave sensors. By choosing the right threshold values for the NDWI and the backscatter, water can be separated from land.

#### HOW CAN DIFFERENT SOURCES OF SATELLITE BASED REMOTE SENSING BE COMBINED IN ONE HYDRODYNAMIC MODEL?

Both optical and microwave images are useful in providing information about the river geometry, because the edge comparison showed that both methods can deviate water from land. Nevertheless the edge locations were shown to be not exactly the same, when examining a day that both optical and SAR data was available, see Figure 5.56. By choosing the optimal thresholds, the locations of the edges can come very close to each other but they still follow a slightly different path, see Section 5.4. If the error margin between both methods is taken into account the images can be combined for hydrodynamic modelling. Another option to combine the sources in one hydrodynamic model is to mostly use the optical images and only use the Sentinel-1 images during the monsoon when there are no clear optical images available because of the clouds.

### WHAT IS THE SPATIAL-TEMPORAL RESOLUTION WHEN COMBINING OPTICAL SATELLITE IMAGES WITH MICROWAVE SATELLITES IMAGES?

When combining Landsat 8, Sentinel-2 and Sentinel-1, the average revisit period becomes 5 days, as shown in Table 5.1. This does not mean that exactly every five days a new image is available. The maximum time period between acquisitions is 21 days and the shortest time period is 0 days, because there can be two acquisitions taken on the same day by different satellites. When the time gap in the data becomes larger, the hydrodynamic model predictions could become less reliable. When the river shows a very steady yearly (seasonal) trend, the data gaps might be partly covered by using this trend.

The spatial resolution of Landsat 8 is 30 meter and the Sentinel satellites have a spatial resolution of 10 meter. For this thesis all images were resampled which made the images smoother and increased the spatial resolution as shown in Section 4.2. Furthermore the spatial resolution depended on choosing the right threshold value. In the sensitivity analysis on thresholding in Section 5.4, for different threshold values of the NDWI and backscatter the resulting edge locations were plotted. For the NDWI this resulted in a variation of 2-5 meters when the NDWI varied by 0.1. For the backscatter the variation in edge location is between 2-5 meters when the threshold is varied with 1 dB.

### HOW ARE RIVER GEOMETRY AND DISCHARGE RELATED?

In Figure 5.58 the relation between the discharge and river area for the Katha polygon in the period 1996-2010 is plotted. This figure shows that in general there is a linear relation between the river area and the discharge. Nevertheless the figure shows a large spread in measurements, which indicates that the relation might change due to changes in the river morphology. After the large flood events that happen each year during the monsoon the river geometry within the Katha geometry might have changed so that for the same discharge in one year the river area might be different in another year.

### WHICH VALIDATION DATA IS AVAILABLE?

To validate the results, the area estimations based on optical images were compared to the area estimations based on microwave images in Figure 5.61. The problem is that for the period 2014-2019 only 27 days were available during which both a Sentinel-1 image and a 'clear' Landsat 8 or Sentinel-2 image was available. So for validation if using optical images gives similar area estimations to using microwave images, the time series in Figure 5.28 and Figure 5.27 can be used instead. This figures show that for both the fixed thresholding and the Otsu thresholding, the time series of the optical and microwave images do not overlap entirely. As explained in Chapter 6 this mismatch can be caused by the noise in the Sentinel-1 images.

## 7.2. RECOMMENDATIONS

### 7.2.1. RECOMMENDATIONS FOR FUTURE RESEARCH

#### USING MORE (DIFFERENT) DATA SOURCES

Next to using more satellites that provide optical or microwave images, it might be useful to extend this research with other data sources. For example, it might be useful to use Digital Elevation Models (DEM's) to define the maximum edges of the rivers by measuring where the levees are located, which are natural dikes preventing the river from flooding up to a certain discharge. Furthermore it might be useful to investigate if it is possible to use Landsat-7 by finding a way to deal with the SLC failure.

#### PERFORM OUTLIER DETECTION

Some of the NDWI or backscatter distributions were not bimodal or the two distributions of the water and the non-water pixels showed a lot of overlap, making it difficult to find the right threshold value. More investigation is needed to find the causes of when the threshold value is reliable and how large the error margin is.

### CORRECT THE SENTINEL-1 NOISE

In the Sentinel-1 images there is a lot of noise which causes pixels outside of the river to be falsely classified as water, as shown in Figure 5.56. The area estimations would be more precise if this noise could be removed. One way of removing this noise is classifying each polygon separately, all polygons smaller than a certain area are classified as non-water and only the water pixels that represent the river will be taken into account. Also other existing algorithms that deal with noise could be investigated.

### TEST THE METHOD ON OTHER LOCATIONS

The Irrawaddy river is a very dynamic river with a lot of variations in discharge and morphodynamics. To investigate if this method is more widely applicable the method should be tested at other locations around the world.

### INVESTIGATING WHAT CAN INFLUENCE THRESHOLDING AND AREA ESTIMATIONS

In Section 5.4 the sensitivity of thresholds was investigated. It was concluded that when choosing the wrong threshold, this influences the the area estimation. In this case it was assumed that with the right threshold water and non-water pixels could perfectly be distinguished. Nevertheless it was not taken into account that sometimes pixels could have a value above the threshold values, whereas this pixel does not belong to the river. For example, when the ground is very saturated the pixel can be falsely classified as water. Or the other way around, when the river is covered with vegetation, the river can be falsely classified as land.

#### 7.2.2. RECOMMENDATIONS FOR USE

Following Huang *et al.* (2018), the MNDWI is more stable than the NDWI. Nevertheless this thesis showed that in the region around Katha there is not much of a difference between the results of using the two indices. Nevertheless at other locations around the world it can have a big influence which water index to use. For example, if the water contains a lot of sediments or other optical active constituent the MNDWI would be more stable because the 'swir' band is less sensitive to constituents than the 'nir' band. The limitation of the MNDWI is that it can not discriminate water and snow, so in areas with snow it is recommended to use the NDWI.

In this thesis, both the fixed threshold and the flexible Otsu thresholding were used. The flexible threshold showed better results ant therefore it is recommended to use Otsu thresholding instead of a fixed threshold. The Otsu thresholding should be performed after the Canny Edge detector is applied.

To avoid the problem that the area estimations based on the Sentinel-1 images are much higher than the area estimations based on the multispectral images it could be recommended to use the multispectral images outside of the monsoon and the Sentinel-1 images to fill the gap of images during the monsoon.





# HYDRODYNAMICS

## A.0.1. FLOW REGIMES

Some knowledge about the different flow regimes is necessary when working with hydrodynamic models. When flow is "steady" it means that the flow is stationary and temporally constant, there are no changes in flow velocity and flow depth over time. Furthermore the flow can be uniform or non-uniform. When the flow is uniform, the flow is spatially constant. Under normal flow or equilibrium flow there is a balance between the resistance force and the downstream component of the gravitational force. As a result the water surface is parallel to the bed surface and there are no accelerations or decelerations and this indicates that the flow is steady and uniform. When a river is in equilibrium the bed level does not change and the transport rate does not vary spatially. In a steady state the river bed has adjusted such that all sediment that is supplied upstream is transported in the downstream direction. Nevertheless, there are a lot of reasons why generally the flow is not normal. There can be naturally temporal variation in flow rate (flood event), a spatial variation in channel pattern, width or friction, confluences, bifurcations or a change in sea level. Furthermore human induced factors, such as dams and other structures, influence the flow rate.

## A.0.2. CONTINUITY EQUATIONS

The water flow in 1D hydrodynamic modelling can be computed by solving the unidirectional form of the shallow water equations, named 1-D Saint-Venant equations. These 1D Saint-Venant equations can be derived from the Navier-Stokes equations that describe fluid motion. For one dimensional flow the 1D continuity equation (Eq. A.1) and the 1D momentum equation (Eq. A.2) need to be solved. These equations are based on the following assumptions from [Crosato \(2016\)](#):

- The flow is one-dimensional.
- The pressure is hydrostatic.
- The effects of boundary friction and turbulence can be accounted for through resistance laws analogous to those used for steady flow.
- The average channel bed slope is small.

The 1D continuity equation (Eq. A.1) is based on the "Conservation of Mass", which states that in any control volume the net change of mass due to inflow and outflow is equal to the net rate of change of mass in the control volume. In this equation,  $A$  is the cross-sectional flow area,  $Q$  the water discharge and  $q_{lat}$  the water discharge per unit length.

$$\frac{\delta A}{\delta t} + \frac{\delta Q}{\delta x} = q_{lat} \quad (A.1)$$

The 1D momentum equation (Eq. A.2) is based on the "Conservation of Momentum", where  $h$  is the water level,  $R_h$  is the hydraulic radius,  $W$  is the width of the water surface,  $\tau_{wind}$  the wind shear stress,  $\rho_w$  the density of water,  $\xi$  an extra resistance coefficient,  $g$  the gravitational acceleration,  $C$  the Chézy coefficient and  $L_x$  the length of the branch segment.

$$\frac{\delta Q}{\delta t} + \frac{\delta}{\delta x} \frac{Q^2}{A} + gA \frac{\delta h}{\delta x} + \frac{gQ|Q|}{C^2 R_h A} - W \frac{\tau_{wind}}{\rho_w} + gA \frac{\xi|Q|}{L_x} = 0 \quad (\text{A.2})$$

The momentum equation represents, in the same order as equation A.2, the following terms:

$$\textit{inertia} + \textit{convection} + \textit{water level gradient} + \textit{bed friction} + \textit{wind force} + \textit{extra resistance} = 0. \quad (\text{A.3})$$

The full momentum equation is used when the flow is unsteady and non-uniform. If the flow is steady, all terms which vary in time can be neglected, which in this case is the inertia term. When the flow is uniform there are no changes over distance, so the convection term become zero. Furthermore the pressure is assumed to be hydrostatic, so the water level gradient term becomes zero. In the end only the friction and force terms remain for steady, uniform flow.

Under normal flow conditions the conservation of water mass can be used to relate the discharge per unit width  $q_w$  to the flow velocity  $u$  and flow depth  $d$ . This relation can be rewritten to relate the water discharge  $Q$  to water discharge per unit width  $q_w$  and the river width  $W$  as shown in Eq. A.5.

$$q_w = ud \quad (\text{A.4})$$

$$Q = q_w W \quad (\text{A.5})$$

The Manning and Chézy's equations are used to describe the resistance effects when using the Saint-Venant equations. In the Chézy equation (Eq. A.6),  $C$  is the Chézy coefficient,  $d$  is the river depth,  $i_b$  is the river bed gradient and  $u$  the flow velocity.

$$u = C \sqrt{d i_b} \quad (\text{A.6})$$

In the Manning equation (Eq. A.7),  $V$  is the cross-sectional average velocity,  $k_n = 1$  for the international system of units,  $R_h$  is the hydraulic radius and  $i_b$  is the slope of the river bed.

$$V = \frac{k_n}{n} R_h^{\frac{2}{3}} i_b^{\frac{1}{2}} \quad (\text{A.7})$$

In Finnegan *et al.* (2005) an expression is formulated (Eq. A.8), based on the Manning equation, which scales the steady state width as a function of discharge  $Q$ , channel slope  $i_b$ , roughness  $n$ , and width-to-depth ratio  $\alpha$ . In Fisher *et al.* (2013) it is mentioned that this model relies on the assumption that the channel is in steady state and that the effect of the landscape transience and sediment transport and cover variability on channel geometries is neglected.

$$W = [\alpha(\alpha + 2)^{2/3}]^{3/8} Q^{3/8} i_b^{-3/16} n^{3/8} \quad (\text{A.8})$$

### A.0.3. RIVER GEOMETRY EQUATIONS

River cross-sections give information about the topography of the riverbed, which is defined by geometrical parameters. In Figure A.1 the cross-sectional area  $A$ , the river width  $W$ , the wetted perimeter  $P_{wet}$  and the hydraulic radius  $R_h$  are displayed.

Next to the bed slope and the bed roughness, the hydraulic radius controls the water discharge and the amount of work the river can do in moving sediment (see Eq. A.7). The hydraulic radius is the ratio between the cross-sectional area of the flow  $A$  and the wetted perimeter  $P_{wet}$  (eq. A.9).

$$R_h = \frac{A}{P_{wet}} \quad (\text{A.9})$$

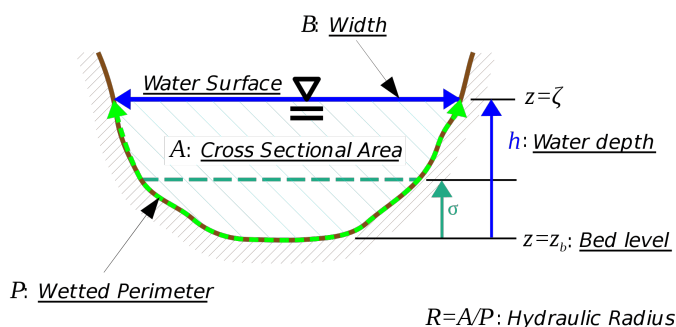


Figure A.1: River cross-section of the open channel. (Wikipedia, 2019b)

When a channel is much wider than it is deep ( $W \gg d$ ), the wetted perimeter becomes almost equal to the channel width and the hydraulic radius approaches the flow depth. The actual width of the river depends on the water level, which varies over time as a result of varying discharge. The bank-full width is the maximum width the river can reach before the water level becomes too high and the water flows over the (natural) levees into the floodplain as shown in Figure A.2.

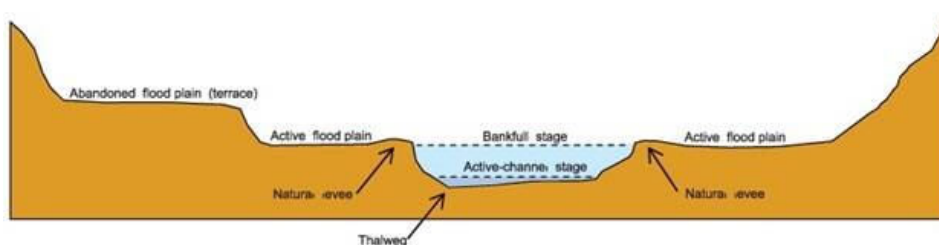


Figure A.2: Schematic diagram showing the geomorphic features of a stream channel. (Sherwood and Huitger, 2005)

In Sichangi *et al.* (2016) three ideal river cross-sections were chosen to relate river discharge to river geometry, see Figure A.3. The method starts with rewriting the Manning's equation (Eq. A.7) to:

$$q_w = \frac{1}{n} A \left( \frac{A}{P_{wet}} \right)^{\frac{2}{3}} i_b^{\frac{1}{2}}. \quad (\text{A.10})$$

For every cross-section the wetted perimeter  $P_{wet}$  and cross-sectional area  $A$  can be written in terms of width  $W$  and depth  $d$  to get discharge equations based on width, depth, slope and Manning's roughness. These equations are not given here, but can be found in Sichangi *et al.* (2016). In case the river is very large, so  $W \gg d$ , for all cross-sections you can use the approximation given in Eq. A.11.

$$q_w \approx \frac{1}{v} i_b^{\frac{1}{2}} W d^{\frac{3}{5}} \quad (\text{A.11})$$

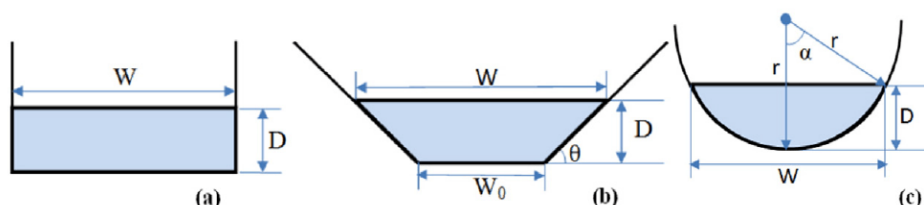


Figure A.3: Three ideal river cross-sections. (Sichangi *et al.*, 2016)

For rivers that are not straight the curvature ratio ( $\gamma$ ) is defined as the ratio between the bankfull channel width ( $B$ ) and the radius of curvature of the channel centerline ( $R_c$ ), see Eq. A.12 and Figure A.4. Following [Crosato \(2008\)](#) for a mild curvature  $\gamma$  has a value of 0.1 or lower and sharper bends have a value of 1.

$$\gamma = \frac{B}{R_c} \quad (\text{A.12})$$

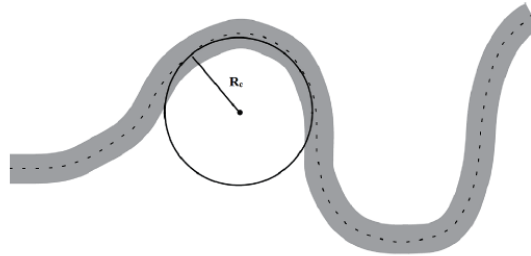


Figure A.4: Radius of curvature of channel centerline ([Zervakis \(2015\)](#))

## LIST OF VARIABLES

Because the same variables are used more often, a list is provided of the different variables to not have to explain them for every equation again. At the original source of the equations, sometimes other characters are used than in this thesis. The characters for some variables are adjusted to get consistency throughout this thesis.

Variable	Description	Units
$\alpha$	Width to depth ratio	–
$A$	Cross-sectional flow area	$m^2$
$B$	Stream Width	$m$
$C$	Chézy coefficient	$m^{1/2}/s$
$c_f$	Dimensionless friction coefficient	1
$d$	flow depth	$m$
$d_e$	Normal flow depth	$m$
$Fr$	Froude number	–
$g$	Gravitational acceleration	$m/s^2$
$h$	Water level	$m$
$i_b$	Streamwise bed slope	1
$k_s$	Channel steepnes index	–?
$L_x$	Length branch segment	$m$
$n$	Roughness (Manning)	$s/m^{1/3}$
$q_w$	Water discharge per unit width	$m^2/s$
$q_{lat}$	lateral discharge per unit length	$m^2/s$
$Q_w$	Water discharge	$m^3/s$
$R_h$	Hydraulic radius	$m$
$\rho_w$	Density of water	$kg/m^3$
$t$	Time	$s$
$\tau_b$	Bed shear stress	$kg/m/s^2$
$\tau_{wind}$	Wind shear stress	$N/m^2$
$u$	Flow velocity	$m/s$
$W$	River width	$m$
$\theta$	Convavity index	–
$\xi$	Extra resistance coefficient	$s^2/m^5$

# BIBLIOGRAPHY

- A. Karpatne, A. Khandelwal, X. Chen, V. Mithal, J. Faghmous, and V. Kumar, *Global monitoring of inland water dynamics: State-of-the-art, challenges, and opportunities*. Computational Sustainability , 121 (2016).
- S. Grimaldi, Y. Li, J. Walker, and V. Pauwels, *Effective representation of river geometry in hydraulic flood forecast models*, *Water Resources Research* **54**, 1031 (2018).
- C. J. Gleason and L. C. Smith, *Toward global mapping of river discharge using satellite images and at-many-stations hydraulic geometry*, *Proceedings of the National Academy of Sciences* **111**, 4788 (2014).
- S. Harada and S. S. Li, *Combining remote sensing with physical flow laws to estimate river channel geometry*, *River Res Applic* **34**, 697 (2018).
- C. Huang, S. Chen, Yun an dZhang, and J. Wu, *Detecting, extracting, and monitoring surface water from space using optical sensors: A review*, *Reviews of Geophysics* **56**, 333 (2018).
- J. J. M. Thissen, *Automating surface water detection for rivers*, Master's thesis, University of Twente (2019).
- G. Donchyts, *Planetary-scale surface water detection from space*, *Ph.D. thesis*, Technical University Delft (2018).
- P. D. Bhavsar, *Review of remote sensing applications in hydrology and water resources management in india*. *Advances in Space Research* **4**, 193 (1984).
- S. K. McFeeters, *The use of the Normalized Difference Water Index (NDWI) in the delineation of open water features*, *International Journal of Remote Sensing* **17**, 1425 (1996).
- X. Hanqiu, *Modification of normalised difference water index (NDWI) to enhance open water features in remotely sensed imagery*, *International Journal of Remote Sensing* **27**, 3025 (2006).
- G. J. P. Schumann and D. K. Moller, *Microwave remote sensing of flood inundation*. *Physics and Chemistry of the Earth* , 83 (2015).
- G. Allen, C. David, K. Andreadis, and J. Hossain, Fand Famiglietti, *Global estimates of river flow wave travel times and implications for low-latency satellite data*, *Geophysical Research Letters* **45**, 7551–7560 (2018).
- A. W. Sichangi, L. Wang, K. Yang, D. Chen, Z. Wang, X. Li, J. Zhou, W. Liu, and D. Kuria, *Estimating continental river basin discharges using multiple remote sensing data sets*, *Remote Sensing of Environment* **179**, 36 (2016).
- B. LibreTexts, *Water Cycle*, <https://bio.libretexts.org/Bookshelves> (2018), 2019-01-25.
- Wikipedia, *Landsat program* — *Wikipedia, the free encyclopedia*, <http://en.wikipedia.org/w/index.php?title=Landsat%20program&oldid=912700714> (2019a), [Online; accessed 30-August-2019].
- USGS, *Comparison of landsat 7 and 8 with sentinel-2*, .
- ESA, *User guides - sentinel-1 sar*, <https://sentinel.esa.int/web/sentinel/user-guides/sentinel-1-sar>, [Online; accessed: 23-August-2019].
- A. Hardy, G. Ettritch, D. E. Cross, P. Bunting, F. Liywalii, S. A. Sakala, Jacob and, D. Singini, M. Smith, T. Willis, and C. J. Thomas, *Automatic detection of open and vegetated water bodies using sentinel 1 to map african malaria vector mosquito breeding habitats*, *Remote Sensing* **11**, 593 (2019).
- P. W. Vachon and J. Wolfe, *C-band cross-polarization wind speed retrieval*. *IEEE Geoscience and Remote Sensing Letters* **8**, 456 (2011).

- Insar at a glance*, <https://site.tre-altamira.com/insar/>, [Online; accessed 30-August-2019].
- J.-F. Pekel, A. Cottam, N. Gorelick, and A. S. Belward, *High-resolution mapping of global surface water and its long-term changes*, *Nature* **450**, 418 (2016).
- GRDC, *Welcome to the global runoff data centre*, [https://www.bafg.de/GRDC/EN/Home/homepage\\_node.html](https://www.bafg.de/GRDC/EN/Home/homepage_node.html) (2019), [Online; accessed 23-April-2019].
- G. Allen and T. Pavelsky, *Global extent of rivers and streams*, *Science* **361**, 585 (2018).
- S. Biancamaria, D. P. Lettenmaier, and T. M. Pavelsky, *The swot mission and its capabilities for land hydrology*, *Surveys in Geophysics* **37**, 307 (2016).
- A. Fisher, N. Flood, and T. Danaher, *Comparing landsat water index methods for automated water classification in eastern australia*, *Remote Sensing of Environment* **175**, 167 (2016).
- S. Solbø, *Towards operational flood mapping with satellite sar*, ResearchGate (2005).
- P. Perona and J. Malik, *Scale-space and edge detection using anisotropic diffusion*, *IEEE Transactions on pattern analysis and machine intelligence* **12**, 629 (1990).
- Z. L. Ji, L. and B. Wylie, *Analysis of dynamic thresholds for the normalized difference water index*. *Photogrammetric Engineering and Remote Sensing* **75**, 1307 (2009).
- N. Otsu, *A threshold selection method from gray-level histograms*, *Automatica* **11**, 285 (1975).
- R. Keys, *Cubic convolution interpolation for digital image processing*, *IEEE Transactions on Acoustics, Speech, and Signal Processing* **29**, 1153 (1981).
- J. Canny, *A computational approach to edge detection*, *IEEE Transactions on pattern analysis and machine intelligence* **6**, 679–698 (1986).
- D. Ringwald, *Edge detection in opencv 4.0, a 15 minutes tutorial*, <https://blog.sicara.com/opencv-edge-detection-tutorial-7c3303f10788> (2012), [Online; accessed 30-August-2019].
- G. Chander, B. L. Markham, and D. L. Helder, *Summary of current radiometric calibration coefficients for landsat mss, tm, etm+, and eo-1 ali sensors*, *Remote Sensing of Environment* **113**, 893 (2009).
- M. Panchagnula, K. , L. Prasanna, B. Chandra Mohan, R. Goru Srinivasa, and B. Veerubhotla, *Optimization of threshold ranges for rapid flood inundation mapping by evaluating backscatter profiles of high incidence angle sar images*. *Int. J. Disaster Risk Sci.* **3**, 113 (2012).
- D. Astaraky, *Time series analysis in r - decomposing time series*, <https://rpubs.com/davoodastaraky/TSA1>, [Online; accessed 28-September-2019].
- J. P. Guerschman, G. Warren, G. Byrne, L. Lymburner, N. Mueller, and A. Van Dijk, *Modis-based standing water detection for flood and large reservoir mapping: algorithm development and applications for the australian continent*. CSIRO: Water for a Healthy Country National Research Flagship Report , 100 (2011).
- A. Crosato, *Applied river morphodynamics: morphological response at the reach scale*, (2016).
- N. J. Finnegan, G. Roe, D. R. Montgomery, and B. Hallet, *Controls on the channel width of rivers: Implications for modeling fluvial incision of bedrock*, *Geology* **33**, 229 (2005).
- B. G. Fisher, B. Bookhagen, and C. B. Amos, *Channel planform geometry and slopes from freely available high-spatial resolution imagery and DEM fusion: Implications for channel width scalings, erosion proxies, and fluvial signatures in tectonically active landscapes*, *Geomorphology* **194**, 46 (2013).
- Wikipedia, *Shallow water equations* — Wikipedia, the free encyclopedia, <http://en.wikipedia.org/w/index.php?title=Shallow%20water%20equations&oldid=906715647> (2019b), [Online; accessed 18-April-2019].
- J. Sherwood and C. Huitger, *Bankfull characteristics of Ohio streams and their relation to peak streamflows: U.S. Geological Survey Scientific Investigations Report 2005-5153*, Tech. Rep. (USGS, 2005).

- 
- A. Crosato, *Analysis and modelling of river meandering*, Ph.D. thesis, Technical University Delft (2008).
- D. I. Zervakis, *Combining a Physics-based Model and Spatial Interpolation of Scarce Bed Topography Data in Meandering Alluvial Rivers*, diploma thesis, Delft University of Technology (2015).